Communications in Applied Mathematics and Computational Science

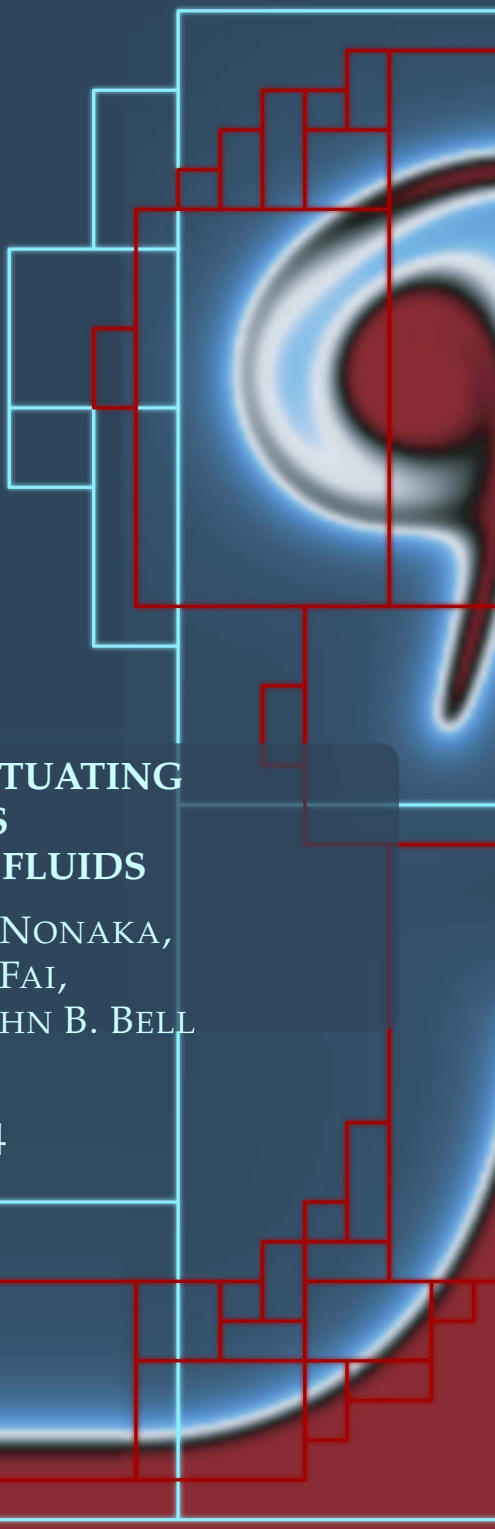

LOW MACH NUMBER FLUCTUATING HYDRODYNAMICS OF DIFFUSIVELY MIXING FLUIDS

ALEKSANDAR DONEV, ANDY NONAKA, YIFEI SUN, THOMAS G. FAI, ALEJANDRO L. GARCIA AND JOHN B. BELL

vol. 9 no. 1 2014

msp

COMM. APP. MATH. AND COMP. SCI.
Vol. 9, No. 1, 2014
dx.doi.org/10.2140/camcos.2014.9.47

LOW MACH NUMBER FLUCTUATING HYDRODYNAMICS OF DIFFUSIVELY MIXING FLUIDS

ALEKSANDAR DONEV, ANDY NONAKA, YIFEI SUN,
THOMAS G. FAI, ALEJANDRO L. GARCIA AND JOHN B. BELL

We formulate low Mach number fluctuating hydrodynamic equations appropriate for modeling diffusive mixing in isothermal mixtures of fluids with different density and transport coefficients. These equations represent a coarse-graining of the microscopic dynamics of the fluid molecules in both space and time and eliminate the fluctuations in pressure associated with the propagation of sound waves by replacing the equation of state with a local thermodynamic constraint. We demonstrate that the low Mach number model preserves the spatiotemporal spectrum of the slower diffusive fluctuations. We develop a strictly conservative finite-volume spatial discretization of the low Mach number fluctuating equations in both two and three dimensions and construct several explicit Runge–Kutta temporal integrators that strictly maintain the equation-of-state constraint. The resulting spatiotemporal discretization is second-order accurate deterministically and maintains fluctuation-dissipation balance in the linearized stochastic equations. We apply our algorithms to model the development of giant concentration fluctuations in the presence of concentration gradients and investigate the validity of common simplifications such as neglecting the spatial nonhomogeneity of density and transport properties. We perform simulations of diffusive mixing of two fluids of different densities in two dimensions and compare the results of low Mach number continuum simulations to hard-disk molecular-dynamics simulations. Excellent agreement is observed between the particle and continuum simulations of giant fluctuations during time-dependent diffusive mixing.

I. Introduction

Stochastic fluctuations are intrinsic to fluid dynamics because fluids are composed of molecules whose positions and velocities are random at thermodynamic scales. Because they span the whole range of scales from the microscopic to the macroscopic [23; 75], fluctuations need to be consistently included in all levels of description. Stochastic effects are important for flows in new microfluidic, nanofluidic, and microelectromechanical devices [7]; novel materials such as nanofluids [79]; and

MSC2010: primary 76T99; secondary 65M08.
Keywords: fluctuating hydrodynamics, low Mach expansion, molecular dynamics, giant fluctuations.

biological systems such as lipid membranes [57], Brownian molecular motors [64], and nanopores [20]; as well as processes where the effect of fluctuations is amplified by strong nonequilibrium effects such as ultraclean combustion, capillary dynamics [16; 68], and hydrodynamic instabilities [55; 14; 44].

One can capture thermal fluctuations using direct particle-level calculations. But even coarse-grained particle methods [59; 22; 23] are computationally expensive because the dynamics of individual particles has time scales significantly shorter than hydrodynamic time scales. Alternatively, thermal fluctuations can be included in the Navier–Stokes equations through stochastic forcing terms as proposed by Landau and Lifshitz [48] and later extended to fluid mixtures [61]. The basic idea of *fluctuating hydrodynamics* is to add a *stochastic flux* corresponding to each dissipative (irreversible, diffusive) flux [62]. This ensures that the microscopic conservation laws and thermodynamic principles are obeyed while also maintaining fluctuation-dissipation balance. Specifically, the equilibrium thermal fluctuations have the Gibbs–Boltzmann distribution dictated by statistical mechanics. Fluctuating hydrodynamics is a useful tool in understanding complex fluid flows far from equilibrium [61], but theoretical calculations are often only feasible after ignoring nonlinearities, inhomogeneities in density, temperature, and transport properties, surface dynamics, gravity, unsteady flow patterns, and other important effects. In the past decade, fluctuating hydrodynamics has been applied to study a number of nontrivial practical problems [31; 68; 71; 3]; however, the numerical methods used are far from the comparable state of the art for deterministic solvers.

Previous computational studies of the effect of thermal fluctuations in fluid mixtures [68; 6; 71] have been based on the compressible fluid equations and thus require small time steps to resolve fast sound waves (pressure fluctuations). Recently, some of us developed finite-volume methods for the incompressible equations of fluctuating hydrodynamics [73], which eliminate the stiffness arising from the separation of scales between the acoustic and vortical modes [47; 52]. For inhomogeneous fluids with nonconstant density, diffusive mass and heat fluxes create local expansion and contraction of the fluid, and the incompressibility constraint should be replaced by a "quasi-incompressibility" constraint [52; 50]. The resulting *low Mach number* equations have been used for some time to model deterministic flows with thermochemical effects [66; 52], and several conservative finite-volume techniques have been developed for solving equations of this type [63; 67; 15; 58; 56]. To our knowledge, thermal fluctuations have not yet been incorporated in low Mach number models.

In this work, we extend the staggered-grid, finite-volume approach developed in [73] to isothermal mixtures of fluids with unequal densities. The imposition of the quasi-incompressibility constraint poses several nontrivial mathematical and computational challenges. At the mathematical level, the traditional low Mach number asymptotic expansions [47; 52] assume spatiotemporal smoothness of the

flow and thus do not directly apply in the stochastic context. At the computational level, enforcing the quasi-incompressibility or equation-of-state (EOS) constraint in a conservative and stable manner requires specialized spatiotemporal discretizations. By careful selection of the analytical form of the EOS constraint and the spatial discretization of the advective fluxes, we are able to maintain strict local conservation and enforce the EOS to within numerical tolerances. In the present work, we employ an explicit projection-based temporal discretization because of the substantial complexity of designing and implementing semi-implicit discretizations of the momentum equation for spatially inhomogeneous fluids [10].

Thermal fluctuations exhibit unusual features in systems out of thermodynamic equilibrium. Notably, external gradients can lead to *enhancement* of thermal fluctuations and to *long-range* correlations between fluctuations [36; 53; 30; 60; 61]. Sharp concentration gradients present during diffusive mixing lead to the development of macroscopic or *giant fluctuations* [77; 72; 9] in concentration, which have been observed using light-scattering and shadowgraphy techniques [76; 12; 75]. These experimental studies have found good but imperfect agreement between the predictions of a simplified fluctuating hydrodynamic theory and experiments. Computer simulations are, in principle, an ideal tool for studying such complex time-dependent processes in the presence of nontrivial boundary conditions without making the sort of approximations necessary for analytical calculations such as assuming spatially constant density and transport coefficients and spatially uniform gradients. On the other hand, the multiscale (more precisely, *many-scale*) nature of the equations of fluctuating hydrodynamics poses many mathematical and computational challenges that are yet to be addressed. Notably, it is necessary to develop temporal integrators that can accurately and robustly handle the large separation of time scales between different physical processes such as mass and momentum diffusion. The computational techniques we develop here form the foundation for incorporating additional physics such as heat transfer and internal energy fluctuations, phase separation and interfacial dynamics, and chemical reactions.

We begin Section II by formulating the fluctuating low Mach number equations for an isothermal binary fluid mixture. We present both a traditional pressure (constrained) formulation and a gauge (unconstrained) formulation. We analyze the spatiotemporal spectrum of the thermal fluctuations in the linearized equations and demonstrate that the low Mach equations eliminate the fast (sonic) pressure fluctuations but maintain the correct spectrum of the slow (diffusive) fluctuations. In Section III, we develop projected Runge–Kutta schemes for solving the spatially discretized equations, including a midpoint and a trapezoidal second-order predictor-corrector scheme and a third-order three-stage scheme. In Section IV, we describe a spatial discretization of the equations that strictly maintains the equation-of-state constraint and also obeys a fluctuation-dissipation balance principle [29]. In

Section V, we study the steady-state spectrum of giant concentration fluctuations in the presence of an applied concentration gradient in a mixture of two dissimilar fluids and test the applicability of common approximations that neglect spatial inhomogeneities. In Section VI, we study the dynamical evolution of giant interface fluctuations during diffusive mixing of two dissimilar fluids, using both hard-disk molecular dynamics and low Mach number fluctuating hydrodynamics. We find excellent agreement between the two, providing a strong support for the usefulness of the fluctuating low Mach number equations as a coarse-grained model of complex fluid mixtures. In Section VII, we offer some concluding remarks and point out several outstanding challenges for the future. Several technical calculations and procedures are detailed in the appendices.

II. Low Mach number equations

The compressible equations of fluctuating hydrodynamics were proposed some time ago [48] and have since been studied and applied successfully to a variety of situations [61]. The presence of rapid pressure fluctuations due to the propagation of sound waves leads to stiffness that makes it computationally expensive to solve the fully compressible equations numerically especially for typical liquids. It is therefore important to develop fluctuating hydrodynamics equations that capture the essential physics in cases where acoustics can be neglected.

It is important to note that the equations of fluctuating hydrodynamics are to be interpreted as a mesoscopic coarse-grained representation of the mass, momentum, and energy transport that occurs at microscopic scales through molecular interactions (collisions). As such, these equations implicitly contain a mesoscopic coarse-graining length and time scale that is larger than molecular scales [34]. While a coarse-graining scale does not appear explicitly in the formal stochastic partial differential equations (SPDEs) written in this section (but note that it can be if desired [26]), it does explicitly enter in the spatiotemporal discretization described in Section IV through the grid spacing (equivalently, the volume of the grid or, more precisely, the number of molecules per grid cell) and time-step size. This changes the appropriate interpretation of convergence of numerical methods to a continuum limit in the presence of fluctuations and nonlinearities [18]. Only for the linearized equations of fluctuating hydrodynamics [61] can the formal SPDEs be given a precise continuum meaning [29].

Developing coarse-grained models that only resolve the relevant spatiotemporal scales is a well-studied but still ad hoc procedure that requires substantial a priori physical insight [62]. More precise mathematical mode-elimination procedures [39; 40; 41; 45] are technically involved and often purely formal especially in the context of SPDEs [26]. Here we follow a heuristic approach to constructing

fluctuating low Mach number equations, starting from the well-known deterministic low Mach equations (which can be obtained via asymptotic analysis [47; 52]) and then adding fluctuations in a manner consistent with fluctuation-dissipation balance. Alternatively, our low Mach number equations can be seen as a formal asymptotic limit in which the noise terms are formally treated as smooth forcing terms; a more rigorous derivation is nontrivial and is deferred for future work.

II-A. ***Compressible equations.*** The starting point of our investigations is the system of isothermal compressible equations of fluctuating hydrodynamics for the density $\rho(\boldsymbol{r}, t)$, velocity $\boldsymbol{v}(\boldsymbol{r}, t)$, and mass concentration $c(\boldsymbol{r}, t)$ for a mixture of two fluids in d dimensions. In terms of mass and momentum densities, the equations can be written as conservation laws [62; 61; 6]

$$\begin{aligned}
\partial_t \rho + \boldsymbol{\nabla} \cdot (\rho \boldsymbol{v}) &= 0, \\
\partial_t (\rho \boldsymbol{v}) + \boldsymbol{\nabla} \cdot (\rho \boldsymbol{v}\boldsymbol{v}^T) &= -\boldsymbol{\nabla} P + \rho \boldsymbol{g} \\
&\quad + \boldsymbol{\nabla} \cdot \Big[\eta (\boldsymbol{\nabla} \boldsymbol{v} + \boldsymbol{\nabla}^T \boldsymbol{v}) + \Big(\kappa - \frac{2}{d} \eta \Big) (\boldsymbol{\nabla} \cdot \boldsymbol{v}) \boldsymbol{I} + \boldsymbol{\Sigma} \Big], \\
\partial_t (\rho_1) + \boldsymbol{\nabla} \cdot (\rho_1 \boldsymbol{v}) &= \boldsymbol{\nabla} \cdot [\rho \chi (\boldsymbol{\nabla} c + K_P \boldsymbol{\nabla} P) + \boldsymbol{\Psi}],
\end{aligned} \tag{1}$$

where $\rho_1 = \rho c$ is the density of the first component, $\rho_2 = (1 - c)\rho$ is the density of the second component, $P(\rho, c; T)$ is the equation of state for the pressure at the reference temperature $T = T_0 = \text{const}$, and $\boldsymbol{g}$ is the gravitational acceleration. Temperature fluctuations are neglected in this study but can be accounted for using a similar approach. The shear viscosity η, bulk viscosity κ, mass diffusion coefficient χ, and barodiffusion coefficient K_P, in general, depend on the state. The barodiffusion coefficient K_P above (denoted by k_P/P in [6]; see Equation (A.17) there) is not a transport coefficient but rather determined from thermodynamics [49] as

$$K_P = \frac{(\partial \mu / \partial P)_c}{(\partial \mu / \partial c)_P} = -\rho^{-2} \frac{(\partial \rho / \partial c)_P}{(\partial \mu / \partial c)_P} = \frac{(\partial P / \partial c)_\rho}{\rho^2 c_T^2 \mu_c}, \tag{2}$$

where μ is the chemical potential of the mixture at the reference temperature, $\mu_c = (\partial \mu / \partial c)_P$, and $c_T^2 = (\partial P / \partial \rho)_c$ is the isothermal speed of sound. The capital Greek letters denote stochastic momentum and mass fluxes that are formally modeled as [73]

$$\begin{aligned}
\boldsymbol{\Sigma} &= \sqrt{\eta k_B T} \Big(\boldsymbol{\mathcal{W}} + \boldsymbol{\mathcal{W}}^T - \frac{2}{d} \operatorname{Tr} \boldsymbol{\mathcal{W}} \Big) + \sqrt{\frac{2 \kappa k_B T}{d}} \operatorname{Tr} \boldsymbol{\mathcal{W}}, \\
\boldsymbol{\Psi} &= \sqrt{2 \chi \rho \mu_c^{-1} k_B T}\, \widetilde{\boldsymbol{\mathcal{W}}},
\end{aligned} \tag{3}$$

where k_B is Boltzmann's constant and $\boldsymbol{\mathcal{W}}(\boldsymbol{r}, t)$ and $\widetilde{\boldsymbol{\mathcal{W}}}(\boldsymbol{r}, t)$ are standard zero-mean, unit-variance random Gaussian tensor and vector fields with uncorrelated components

$$\langle \mathcal{W}_{ij}(\boldsymbol{r}, t)\mathcal{W}_{kl}(\boldsymbol{r}', t')\rangle = \delta_{ik}\,\delta_{jl}\,\delta(t-t')\,\delta(\boldsymbol{r}-\boldsymbol{r}')$$

and similarly for $\widetilde{\boldsymbol{\mathcal{W}}}$.

II-B. ***Low Mach equations.*** At mesoscopic scales, in typical liquids, sound waves are much faster than momentum diffusion and can usually be eliminated from the fluid-dynamics description. Formally, this corresponds to taking the zero-Mach-number singular limit $c_T \to \infty$ of the system (1) by performing an asymptotic analysis as the Mach number $\mathrm{Ma} = U/c_T \to 0$, where U is a reference flow velocity. The limiting dynamics can be obtained by performing an asymptotic expansion in the Mach number [47]. In a deterministic setting, this analysis shows that the pressure can be written in the form

$$P(\boldsymbol{r}, t) = P_0(t) + \pi(\boldsymbol{r}, t),$$

where $\pi = O(\mathrm{Ma}^2)$. The low Mach number equations can then be obtained by making the ansatz that the thermodynamic behavior of the system is captured by the reference pressure, P_0, and π captures the mechanical behavior while not affecting the thermodynamics. We note that, when the system is sufficiently large or the gravitational forcing is sufficiently strong, assuming a spatial constant reference pressure is not valid. In those cases, the reference pressure represents a global hydrostatic balance $\nabla P_0 = \rho_0 \boldsymbol{g}$ (see [32] for details of the construction of these types of models). Here, however, we will restrict consideration to cases where gravity causes negligible changes in the thermodynamic state across the domain.

In this case, the reference pressure constrains the system so that the evolution of ρ and c remains consistent with the thermodynamic equation of state

$$P\big(\rho(\boldsymbol{r}, t), c(\boldsymbol{r}, t); T\big) = P_0(t). \tag{4}$$

This constraint means that any change in concentration (equivalently, ρ_1) must be accompanied by a corresponding change in density as would be observed in a system at thermodynamic equilibrium held at the fixed reference pressure and temperature. This implies that variations in density are coupled to variations in composition. Note that we do not account for temperature variations in our isothermal model.

The equation for ρ_1 can be written in primitive (nonconservation) form as the concentration equation

$$\rho \frac{Dc}{Dt} = \rho D_t c = \rho(\partial_t c + \boldsymbol{v}\cdot\nabla c) = \nabla\cdot\boldsymbol{F}, \tag{5}$$

where the nonadvective (diffusive and stochastic) fluxes are denoted with

$$\boldsymbol{F} = \rho\chi\nabla c + \boldsymbol{\Psi}.$$

Note that there is no barodiffusion flux because barodiffusion is of thermodynamic origin (as seen from (2) [61]) and involves the gradient of the *thermodynamic* pressure $\nabla P_0 = 0$. By differentiating the EOS constraint along a Lagrangian trajectory, we obtain

$$\frac{D\rho}{Dt} = \beta\rho\frac{Dc}{Dt} = \beta\nabla\cdot\boldsymbol{F} = \partial_t\rho + \boldsymbol{v}\cdot\nabla\rho = -\rho\nabla\cdot\boldsymbol{v}, \tag{6}$$

where the solutal expansion coefficient

$$\beta(c) = \frac{1}{\rho}\Big(\frac{\partial\rho}{\partial c}\Big)_{P_0}$$

is determined by the specific form of the EOS.

Equation (6) shows that the EOS constraint can be rewritten as a constraint on the divergence of velocity,

$$\rho\nabla\cdot\boldsymbol{v} = -\beta\nabla\cdot\boldsymbol{F}. \tag{7}$$

Note that the usual incompressibility constraint is obtained when the density is not affected by changes in concentration, $\beta = 0$. When $\beta \neq 0$, changes in composition (concentration) due to diffusion cause local expansion and contraction of the fluid and thus a nonzero $\nabla\cdot\boldsymbol{v}$. It is important at this point to consider the boundary conditions. For a closed system, such as a periodic domain or a system with rigid boundaries, we must ensure that the integral of $\nabla\cdot\boldsymbol{v}$ over the domain is zero. This is consistent with (7) if β/ρ is constant so that we can rewrite (7) in the form $\nabla\cdot\boldsymbol{v} = -\nabla\cdot((\beta/\rho)\boldsymbol{F})$. In this case, P_0 does not vary in time. If β/ρ is not constant, then for a closed system the reference pressure P_0 must vary in time to enforce that the total fluid volume remains constant. Here we will assume that $\beta/\rho = \text{const}$, and we will give a specific example of an EOS that obeys this condition.

The asymptotic low Mach analysis of (1) is standard and follows the procedure outlined in [47], formally treating the stochastic forcing as smooth. This analysis leads to the *isothermal low Mach number* equations for a binary mixture of fluids in conservation form,

$$\partial_t(\rho\boldsymbol{v}) + \nabla\pi = -\nabla\cdot(\rho\boldsymbol{v}\boldsymbol{v}^T) + \nabla\cdot[\eta(\nabla\boldsymbol{v} + \nabla^T\boldsymbol{v}) + \boldsymbol{\Sigma}] + \rho\boldsymbol{g} \equiv \boldsymbol{f}(\rho, \boldsymbol{v}, c, t), \tag{8}$$

$$\partial_t(\rho_1) = -\nabla\cdot(\rho_1\boldsymbol{v}) + \nabla\cdot\boldsymbol{F} \equiv h(\rho, \boldsymbol{v}, c, t), \tag{9}$$

$$\partial_t(\rho_2) = -\nabla\cdot(\rho_2\boldsymbol{v}) - \nabla\cdot\boldsymbol{F}, \tag{10}$$

$$\text{such that } \nabla\cdot\boldsymbol{v} = -(\rho^{-1}\beta)\nabla\cdot\boldsymbol{F} \equiv S(\rho, c, t). \tag{11}$$

The gradient of the nonthermodynamic component of the pressure π (Lagrange multiplier) appears in the momentum equation as a driving force that ensures the EOS constraint (11) is obeyed. We note that the bulk viscosity term gives a gradient term that can be absorbed in π and therefore does not explicitly need to appear in the equations. By adding the two density equations (9) and (10), we get the usual continuity equation for the total density,

$$\partial_t \rho = -\nabla \cdot (\rho \boldsymbol{v}). \tag{12}$$

Our conservative numerical scheme is based on (8), (9), (11), and (12).

In Appendix A, we apply the standard linearized fluctuating hydrodynamics analysis to the low Mach number equations. This gives expressions for the equilibrium and nonequilibrium static and dynamic covariances (spectra) of the fluctuations in density and concentration as a function of wavenumber and wave frequency. Specifically, the dynamic structure factor in the low Mach number approximation has the form

$$S_{\rho,\rho}(\boldsymbol{k}, \omega) = \left\langle (\widehat{\delta\rho})(\widehat{\delta\rho})^\star \right\rangle = \beta^2 (\rho \mu_c^{-1} k_B T) \frac{2\chi k^2}{\omega^2 + \chi^2 k^4}.$$

The linearized analysis shows that the low Mach number equations reproduce the slow fluctuations (small ω) in density and concentration (central Rayleigh peak in the dynamic structure factor [61; 29]) as in the full compressible equations (see Section A.1) while eliminating the fast isentropic pressure fluctuations (side Brillouin peaks) from the dynamics.

The fluctuations in velocity, however, are different between the compressible and low Mach number equations. In the compressible equations, the dynamic structure factor for the longitudinal component of velocity decays to zero as $\omega \to \infty$ because it has two sound (Brillouin) peaks centered around $\omega \approx \pm c_T k$ in addition to the central diffusive (Rayleigh) peak. The low Mach number equations reproduce the central peak (slow fluctuations) correctly, replacing the side peaks with a flat spectrum for large ω, which is unphysical as it formally makes the velocity white in time. The low Mach equations should therefore be used only for time scales larger than the sound propagation time.

The fact that the velocity fluctuations are white in space and in time poses a further challenge in interpreting the nonlinear low Mach number equations, and in particular, numerical schemes may not converge to a sensible limit as the time step goes to zero. In practice, just as the spatial discretization of the equations imposes a spatial smoothing or regularization of the fluctuations, the temporal discretization of the equations imposes a temporal smoothing and filters the problematic large frequencies. In the types of problems we study in this work, the problem concentration fluctuations can be neglected, $\widehat{\boldsymbol{\Psi}} \approx \boldsymbol{0}$, because the

concentration fluctuations are dominated by nonequilibrium effects. If $\widehat{\mathbf{\Psi}} = \mathbf{0}$, the problematic white-in-time longitudinal component of velocity disappears.

Model equation of state. In general, the EOS constraint (4) is a nonlinear constraint. In this work, we consider a specific linear EOS,

$$\frac{\rho_1}{\bar{\rho}_1} + \frac{\rho_2}{\bar{\rho}_2} = \frac{c\rho}{\bar{\rho}_1} + \frac{(1-c)\rho}{\bar{\rho}_2} = 1, \tag{13}$$

where $\bar{\rho}_1$ and $\bar{\rho}_2$ are the densities of the pure component fluids ($c = 1$ and $c = 0$, respectively), giving

$$\beta = \rho\Big(\frac{1}{\bar{\rho}_2} - \frac{1}{\bar{\rho}_1}\Big) = \frac{\bar{\rho}_1 - \bar{\rho}_2}{c\bar{\rho}_2 + (1-c)\bar{\rho}_1}. \tag{14}$$

It is important that for this specific form of the EOS β/ρ is a material constant independent of the concentration. The density dependence (14) on concentration arises if one assumes that the two fluids do not change volume upon mixing. This is a reasonable assumption for liquids that are not too dissimilar at the molecular level. Surprisingly, the EOS (13) is also valid for a mixture of ideal gases since

$$P = P_1 + P_2 = P_0 = nk_BT = (n_1 + n_2)k_BT = \Big(\frac{\rho_1}{m_1} + \frac{\rho_2}{m_2}\Big)k_BT,$$

where m is molecular mass and $n = \rho/m$ is the number density. This is exactly of the form (13) with $\bar{\rho}_1 = m_1P_0/(k_BT) = nm_1$ and $\bar{\rho}_2 = nm_2$.

Even if the specific EOS (13) is not a very good approximation over the entire range of concentration $0 \le c \le 1$, (13) may be a very good approximation over the range of concentrations of interest if $\bar{\rho}_1$ and $\bar{\rho}_2$ are adjusted accordingly. In this case, $\bar{\rho}_1$ and $\bar{\rho}_2$ are not the densities of the pure component fluids but rather fitting parameters that approximate the true EOS in the range of concentrations of interest. For small variations in concentration around some reference concentration $\bar{c}$ and density $\bar{\rho}$, one can approximate $\beta \approx \bar{\rho}^{-1}(\partial\rho/\partial c)_{\bar{c}}$ by a constant and determine appropriate values of $\bar{\rho}_1$ and $\bar{\rho}_2$ from (14) and the EOS (13) evaluated at the reference state. Our specific form choice of the EOS will aid significantly in the construction of simple conservative spatial discretizations that strictly maintain the EOS without requiring complicated nonlinear iterative corrections.

Boundary conditions. Several different types of boundary conditions can be imposed for the low Mach number equations just as for the more familiar incompressible equations. The simplest case is when periodic boundary conditions are used for all of the variables. We briefly describe the different types of conditions that can be imposed at a physical boundary with normal direction n.

For the concentration (equivalently, ρ_1), either Neumann (zero mass flux) or Dirichlet (fixed concentration) boundary conditions can be imposed. Physically,

a Neumann condition corresponds to a physical boundary that is impermeable to mass while Dirichlet conditions correspond to a permeable membrane that connects the system to a large reservoir held at a specified concentration. In the case of Neumann conditions for concentration, both the normal component of the diffusive flux $F_n = 0$ and the advective flux $\rho_1 v_n = 0$ vanish at the boundary, implying that the normal component of velocity must vanish, $v_n = 0$. For Dirichlet conditions on the concentration, however, there will, in general, be a nonzero normal diffusive flux F_n through the boundary. This diffusive flux for concentration will induce a corresponding mass flux as required to maintain the equation of state near the boundary. From the condition (11), we infer the proper boundary condition for the normal component of velocity to be

$$v_n = -(\rho^{-1}\beta)F_n. \tag{15}$$

This condition expresses the notion that there is no net volume change for the fluid in the domain. Note that no additional boundary conditions can be specified for ρ since its boundary conditions follow from those on c via the EOS constraint.

For the tangential component of velocity $\boldsymbol{v}_\tau$, we either impose a no-slip condition $\boldsymbol{v}_\tau = 0$ or a free-slip boundary condition in which the tangential component of the normal viscous stress vanishes,

$$\eta\left(\frac{\partial v_n}{\partial \boldsymbol{\tau}} + \frac{\partial \boldsymbol{v}_\tau}{\partial n}\right) = \mathbf{0}.$$

In the case of zero normal mass flux, $v_n = 0$, the free-slip condition simplifies to a Neumann condition for the tangential velocity, $\partial \boldsymbol{v}_\tau / \partial n = 0$.

II-C. ***Gauge formalism.*** The low Mach number system of equations (8), (9), (11), and (12) is a *constrained* problem. For the purposes of analysis and in particular for constructing higher-order temporal integrators, it is useful to rewrite the constrained low Mach number equations as an *unconstrained* initial-value problem. In the incompressible case, $\nabla \cdot \boldsymbol{v} = 0$, we can write the constrained Navier–Stokes equations as an unconstrained system by eliminating the pressure using a projection-operator formalism. The constraint $\nabla \cdot \boldsymbol{v} = 0$ is a constant linear constraint and independent of the state and of time. However, in the low Mach number equations, the velocity-divergence constraint $\nabla \cdot \boldsymbol{v} = -\beta D_t c$ depends on concentration and also on time when there are additional (stochastic or deterministic) forcing terms in the concentration equation. Treating this type of system requires a more general vector-field decomposition. This more general vector-field decomposition provides the basis for a projection-based discretization of the constrained system. We also introduce a gauge formulation of the system [33] that casts the evolution as a nonlocal unconstrained system that is analytically equivalent to the original

constrained evolution. The gauge formulation allows us to develop higher-order method-of-lines temporal integration algorithms.

Vector-field decomposition. The velocity in the low Mach number equations can be split into two components,

$$\boldsymbol{v} = \boldsymbol{u} + \nabla\zeta,$$

where $\nabla \cdot \boldsymbol{u} = 0$ is a divergence-free (solenoidal or vortical) component, and therefore,

$$\nabla \cdot \boldsymbol{v} = \nabla^2\zeta = S(\rho, c, t).$$

This is a Poisson problem for ζ that is well-posed for appropriate boundary conditions on $\boldsymbol{v}$. Specifically, periodic boundary conditions on $\boldsymbol{v}$ imply periodic boundary conditions for $\boldsymbol{u}$ and ζ. At physical boundaries where a Dirichlet condition (15) is specified for the normal component of the velocity, we set $u_n = 0$ and use Neumann conditions for the Poisson solve, $\partial\zeta/\partial n = v_n$.

We can now define a more general vector-field decomposition that plays the role of the Hodge decomposition in incompressible flow. Given a vector field $\tilde{\boldsymbol{v}}$ and a density ρ, we can decompose $\tilde{\boldsymbol{v}}$ into three components

$$\tilde{\boldsymbol{v}} = \boldsymbol{u} + \nabla\zeta + \rho^{-1}\nabla\psi.$$

This decomposition can be obtained by using the condition $\nabla \cdot \boldsymbol{u} = 0$ and $\nabla^2\zeta = S$, which allows us to define a density-weighted Poisson equation for ψ,

$$\nabla \cdot (\rho^{-1}\nabla\psi) = -\nabla \cdot (\tilde{\boldsymbol{v}} - \nabla\zeta) = -\nabla \cdot \tilde{\boldsymbol{v}} + S(\rho, c, t).$$

Let $\boldsymbol{L}_\rho^{-1}$ denote the solution operator to the density-dependent Poisson problem, formally,

$$\boldsymbol{L}_\rho^{-1} = [\nabla \cdot (\rho^{-1}\nabla)]^{-1},$$

and also define a density-dependent projection operator $\mathcal{P}_\rho$ defined through its action on a vector field $\boldsymbol{w}$,

$$\mathcal{P}_\rho \boldsymbol{w} = \boldsymbol{w} - \rho^{-1}\nabla[\boldsymbol{L}_\rho^{-1}(\nabla \cdot \boldsymbol{w})].$$

This is a well-known variable-density generalization [2] of the constant-density projection operator $\mathcal{P}\boldsymbol{w} = \boldsymbol{w} - \nabla[\nabla^{-2}(\nabla \cdot \boldsymbol{w})]$. We can now write

$$\boldsymbol{u} = \mathcal{P}_\rho(\tilde{\boldsymbol{v}} - \nabla\zeta) = \mathcal{P}_\rho\tilde{\boldsymbol{v}} + \rho^{-1}\nabla[\boldsymbol{L}_\rho^{-1}S(\rho, c, t)] - \nabla\zeta.$$

This gives

$$\boldsymbol{v} = \boldsymbol{u} + \nabla\zeta = \mathcal{R}_S(\tilde{\boldsymbol{v}}),$$

where we have introduced an affine transformation $\mathcal{R}_S(\rho, c, t)$ that depends on ρ, c, and t through $S(\rho, c, t)$ and is defined via its action on a vector field $\boldsymbol{w}$,

$$\mathcal{R}_S(\boldsymbol{w}) = \boldsymbol{w} - \rho^{-1}\nabla[\boldsymbol{L}_\rho^{-1}(\nabla\cdot\boldsymbol{w} - S)]. \tag{16}$$

Note that application of $\mathcal{R}_S$ requires only one Poisson solve and does not actually require computing ζ.

Gauge formulation. The low Mach number system (8), (9), (11), and (12) has the form

$$\begin{aligned}
\partial_t\rho &= -\nabla\cdot(\rho\boldsymbol{v}),\\
\partial_t\boldsymbol{m} + \nabla\pi &= \boldsymbol{f}(c, \boldsymbol{v}, t),\\
\partial_t\rho_1 &= h(c, \boldsymbol{v}, t),\\
\nabla\cdot\boldsymbol{v} &= S(\rho, c, t),
\end{aligned} \tag{17}$$

where $\boldsymbol{m} = \rho\boldsymbol{v}$ is the momentum density and $\boldsymbol{f}$, h, and S are as defined in (8), (9), and (11). At present, we will assume that these functions are smooth functions of time, which is only justified in the presence of stochastic forcing terms in a linearized setting. We note that, for the constrained system, ρ is not an independent variable because of the EOS constraint (13); however, we will retain the evolution of ρ with the implicit understanding that the evolution must be constrained so that ρ and c remain consistent with (13).

To define the gauge formulation, we introduce a new variable

$$\widetilde{\boldsymbol{m}} = \rho\tilde{\boldsymbol{v}} = \boldsymbol{m} + \nabla\psi,$$

where ψ is a *gauge* variable. We note that ψ is not uniquely determined; however, the specific choice does not matter. If we choose the gauge so that $\partial_t\psi = \pi$, then the momentum equation in (17) is equivalent to

$$\partial_t\widetilde{\boldsymbol{m}} = \boldsymbol{f}(\rho, \boldsymbol{v}, c, t).$$

The appropriate boundary conditions for ψ are linked to the boundary conditions on $\boldsymbol{v}$; we set ψ to be periodic if $\boldsymbol{v}$ is periodic and employ a homogeneous Neumann (natural) boundary condition $\partial\psi/\partial n = 0$ if a Dirichlet condition (15) is specified for the normal component of the velocity v_n. Note that, in the spatially discrete staggered formulation that we employ, the homogeneous Neumann condition follows automatically from the boundary conditions on velocity used to define the appropriate divergence and gradient operators in the interior of the domain.

If we know $\widetilde{\boldsymbol{m}}$ and ρ, we can then define $\tilde{\boldsymbol{v}} = \widetilde{\boldsymbol{m}}/\rho$ and compute $\boldsymbol{v} = \mathcal{R}_S(\tilde{\boldsymbol{v}})$, where $\mathcal{R}_S$ is defined in (16). Thus, by using the gauge formulation, we can formally

write the low Mach number equations in the form of an unconstrained initial value problem

$$\partial_t \widetilde{\boldsymbol{m}} = \boldsymbol{f}(\rho(c), \boldsymbol{\mathcal{R}}_S(\tilde{\boldsymbol{v}}), c, t), \tag{18}$$

$$\partial_t \rho_1 = h(\rho(c), \boldsymbol{\mathcal{R}}_S(\tilde{\boldsymbol{v}}), c, t). \tag{19}$$

The utility of the gauge formulation is that, in fact, we do not need to know ψ in order to determine $\boldsymbol{v}$. Therefore, the time-evolution equation for ψ does not actually need to be solved, and in particular, π does not need to be computed. Furthermore, by adopting the gauge formulation, we can directly use a method-of-lines approach for spatially discretizing the system (18)–(19) and then apply standard Runge–Kutta temporal integrators to the resulting system of ordinary (stochastic) differential equations.

It is important to emphasize that the actual independent physical variables in the low Mach formulation (18)–(19) are the vortical (solenoidal) component of velocity $\boldsymbol{u}$ and the concentration c. The density $\rho = \rho(c)$ and the velocity $\boldsymbol{v} = \boldsymbol{u} + \boldsymbol{\nabla}[\boldsymbol{\nabla}^{-2} S(\rho, c, t)]$ are determined from $\boldsymbol{u}$ and c and the constraints; hence, they can formally be eliminated from the system as can be seen in the linearized analysis in Appendix A, which shows that fluctuations in the vortical velocity modes are decoupled from the longitudinal fluctuations.

III. Temporal integration

Our spatiotemporal discretization follows a "method-of-lines" approach in which we first discretize the equations (8), (9), (11), and (12) in space and then integrate the resulting semicontinuum equations in time. Our uniform staggered-grid spatial discretization of the low Mach number equations is relatively standard and is described in Section IV. The main difficulty is the temporal integration of the resulting equations in the presence of the EOS constraint. Our temporal integrators are based on the gauge formulation (18)–(19) of the low Mach equations. The gauge formulation is unconstrained and enables us to use standard temporal integrators for initial-value problems. In the majority of this section, we assume that all of the fields and differential operators have already been spatially discretized and focus on the temporal integration of the resulting initial-value problem.

Because in the present schemes we handle both diffusive and advective fluxes explicitly, the time-step size Δt is restricted by well-known CFL conditions. For fluctuating hydrodynamics applications, the time step is typically limited by momentum diffusion,

$$\alpha_\nu = \frac{\nu \Delta t}{\Delta x^2} < \frac{1}{2d},$$

where d is the number of spatial dimensions and Δx is the grid spacing. The design and implementation of numerical methods that handle momentum diffusion semi-implicitly, as done in [73] for incompressible flow, is substantially more difficult for the low Mach number equations because it requires a variable-coefficient implicit fluid solver. We have recently developed an efficient Stokes solver for solving variable-density and variable-viscosity time-dependent and steady Stokes problems [10], and in future work, we will employ this solver to construct a semi-implicit temporal integrator for the low Mach number equations.

Our temporal discretization will make use of the special form of the EOS and the discretization of mass advection described in Section IV-C in order to strictly maintain the EOS relation (13) between density and concentration in each cell at *all* intermediate values. Therefore, no additional action is needed to enforce the EOS constraint after an update of ρ_1 and ρ. This is, however, only true to within the accuracy of the Poisson solver and also roundoff, and it is possible for a slow drifting off the EOS to occur over many time steps. In Section III-C, we describe a correction that prevents such drifting and ensures that the EOS is obeyed at all times to essentially roundoff tolerance. For simplicity, we will often omit the explicit update for the density ρ and instead focus on updating ρ_1 and the momentum density $\boldsymbol{m} = \rho \boldsymbol{v}$ with the understanding that ρ is updated whenever ρ_1 is.

III-A. ***Euler scheme.*** The foundation for our higher-order explicit temporal integrators is the first-order Euler method applied to the gauge formulation (18)–(19).

Gauge-free Euler update. We use a superscript to denote the time step and the point in time where a given term is evaluated, e.g., $f^n \equiv f_D(\rho^n, \boldsymbol{v}^n, c^n, t^n)$, where f_D denotes the spatial discretization of f with analogous definitions for h^n and S^n. We also denote the time-step size with $\Delta t = t^{n+1} - t^n$. Assume that at the beginning of time step n we know $\widetilde{\boldsymbol{m}}^n$ and we can then compute

$$\boldsymbol{v}^n = \boldsymbol{\mathcal{R}}_S^n(\tilde{\boldsymbol{v}}^n)$$

by enforcing the constraint (17). Here $\boldsymbol{\mathcal{R}}_S^n$ denotes the affine transformation (16) with all terms evaluated at the beginning of the time step so that $\nabla \cdot \boldsymbol{v}^n = S^n$. An Euler step for the low Mach equations then consists of the update

$$\begin{aligned} \rho_1^{n+1} &= \rho_1^n + \Delta t\, h^n, \\ \widetilde{\boldsymbol{m}}^{n+1} &= \widetilde{\boldsymbol{m}}^n + \Delta t\, \boldsymbol{f}^n \end{aligned} \tag{20}$$

together with an update of the density ρ^{n+1} consistent with ρ_1^{n+1}.

At the beginning of the next time step, $\boldsymbol{v}^{n+1}$ will be calculated from $\widetilde{\boldsymbol{m}}^{n+1}$ by applying $\boldsymbol{\mathcal{R}}_S^{n+1}$, and it is only $\boldsymbol{v}^{n+1}$ that will actually be used during time step $n+1$. We therefore do not need to explicitly store $\widetilde{\boldsymbol{m}}^{n+1}$ and can instead replace it with

$\boldsymbol{m}^{n+1} = \rho^{n+1}\boldsymbol{v}^{n+1}$ without changing any of the observable results. This is related to the fact that the gauge is de facto arbitrary and, in the present setting, the gauge formulation is simply a formalism to put the equations in an unconstrained form suitable for method of lines discretization. The difference between $\widetilde{\boldsymbol{m}}$ and $\boldsymbol{m}$ is a (discrete) gradient of a scalar. Since our temporal integrators only use linear combinations of the intermediate values, the difference between the final result for $\widetilde{\boldsymbol{m}}^{n+1}$ and $\boldsymbol{m}^n$ is also a gradient of a scalar and replacing $\widetilde{\boldsymbol{m}}^{n+1}$ with $\boldsymbol{m}^{n+1}$ simply amounts to redefining the (arbitrary) gauge variable. For these reasons, the Euler advance,

$$\begin{aligned} \rho_1^{n+1} &= \rho_1^n + \Delta t\, h^n, \\ \boldsymbol{m}^{n+1} &= \rho^{n+1}\boldsymbol{\mathcal{R}}_S^{n+1}[(\rho^{n+1})^{-1}(\boldsymbol{m}^n + \Delta t\, \boldsymbol{f}^n)], \end{aligned} \tag{21}$$

is analytically equivalent to (20). We will use this form as the foundation for our temporal integrators. The equivalence to the gauge form implies that the update specified by (21) can be viewed as an explicit update in spite of the formal dependence of the update on the solution at both old and new time levels.

Stochastic forcing. Thermal fluctuations cannot be straightforwardly incorporated in (21) because it is not clear how to define $\boldsymbol{\mathcal{R}}_S^{n+1}$. In the deterministic setting, S is a function of concentration and density and can be evaluated pointwise at time level $n+1$. When the white-in-time stochastic concentration flux $\boldsymbol{\Psi}$ is included, however, S cannot be evaluated at a particular point of time. Instead, one must think of $\boldsymbol{\Psi}$ as representing the *average* stochastic flux over a given time interval δt, which can be expressed in terms of the increments $\sqrt{\delta t}\,\widetilde{\boldsymbol{W}}$ of the underlying Wiener processes,

$$\boldsymbol{\Psi}(\delta t, \widetilde{\boldsymbol{W}}) = \sqrt{\frac{2\chi\rho\mu_c^{-1}k_B T}{\delta t\, \Delta V}}\,\widetilde{\boldsymbol{W}},$$

where $\widetilde{\boldsymbol{W}}$ is a collection of normal variates generated using a pseudorandom number generator and ΔV is the volume of the hydrodynamic cells. Similarly, the average stochastic momentum flux over a time step is modeled as

$$\boldsymbol{\Sigma}(\delta t, \boldsymbol{W}) = \sqrt{\frac{\eta k_B T}{\delta t\, \Delta V}}(\boldsymbol{W} + \boldsymbol{W}^T),$$

where $\boldsymbol{W}$ are normal random variates. As described in more detail in [73], stochastic fluxes are spatially discretized by generating normal variates on the faces of the grid on which the corresponding variable is discretized independently at each time step. As mentioned earlier, the volume of the grid cell appears here because it expresses the spatial coarse-graining length scale (i.e., the degree of coarse-graining for which a fluid element with discrete molecules can be modeled by continuous density fields) implicit in the equations of fluctuating hydrodynamics. Similarly,

the time interval $\delta t \sim \Delta t$ expresses the typical time scale at which the mass and momentum transfer can be modeled with low Mach number hydrodynamics.

With this in mind, we first evaluate the velocity divergence associated with the constraint using the particular sample of $\boldsymbol{\Psi}$,

$$S = -(\rho^{-1}\beta)\boldsymbol{\nabla}\cdot[\rho\chi\boldsymbol{\nabla}c + \boldsymbol{\Psi}(\delta t, \widetilde{\boldsymbol{W}})].$$

We then define a discrete affine operator $\boldsymbol{\mathcal{R}}_F(\delta t, \widetilde{\boldsymbol{W}})$ in terms of its action on the momentum $\boldsymbol{m}$

$$[\boldsymbol{\mathcal{R}}_F(\delta t, \widetilde{\boldsymbol{W}})](\boldsymbol{m}) = \rho\boldsymbol{\mathcal{R}}_S(\rho^{-1}\boldsymbol{m}).$$

Using this shorthand notation, the momentum update in (21) in the presence of thermal fluctuations can be written as

$$\boldsymbol{m}^{n+1} = \big[\boldsymbol{\mathcal{R}}_F^{n+1}(\Delta t, \widetilde{\boldsymbol{W}}^{n+1})\big](\boldsymbol{m}^n + \Delta t\, \boldsymbol{f}^n).$$

Observe that this is a conservative momentum update since the application of $\boldsymbol{\mathcal{R}}_F$ subtracts the (discrete) gradient of a scalar from the momentum. In actual implementation, it is preferable to apply $\boldsymbol{\mathcal{R}}_F^{n+1}$ at the beginning of the time step $n+1$, instead of at the end of time step n, once the value S^{n+1} is computed from the diffusive and stochastic fluxes for the concentration.

Euler–Maruyama update. Following the above discussion, we can write an Euler–Maruyama temporal integrator for the low Mach number equations in the shorthand notation,

$$\begin{aligned}
\boldsymbol{m}^n &= [\boldsymbol{\mathcal{R}}_F^n(\Delta t, \widetilde{\boldsymbol{W}}^n)](\widetilde{\boldsymbol{m}}^n),\\
\rho_1^{n+1} &= \rho_1^n + \Delta t\, \bar{h}^n + \check{h}^n(\Delta t, \widetilde{\boldsymbol{W}}^n),\\
\widetilde{\boldsymbol{m}}^{n+1} &= \boldsymbol{m}^n + \Delta t\, \bar{\boldsymbol{f}}^n + \check{\boldsymbol{f}}^n(\Delta t, \boldsymbol{W}^n),
\end{aligned} \tag{22}$$

where $\boldsymbol{W}^n$ and $\widetilde{\boldsymbol{W}}^n$ are collections of standard normal variates generated using a pseudorandom number generator independently at each time step. Here the deterministic increments are written using the shorthand notation

$$\begin{aligned}
\bar{\boldsymbol{f}} &= \boldsymbol{\nabla}\cdot[-\rho\boldsymbol{v}\boldsymbol{v}^T + \eta(\boldsymbol{\nabla}\boldsymbol{v} + \boldsymbol{\nabla}^T\boldsymbol{v})] + \rho\boldsymbol{g},\\
\bar{h} &= \boldsymbol{\nabla}\cdot(-\rho_1\boldsymbol{v} + \rho\chi\boldsymbol{\nabla}c).
\end{aligned}$$

The stochastic increments are written in terms of

$$\begin{aligned}
\check{\boldsymbol{f}}(\delta t, \boldsymbol{W}) &= [\boldsymbol{\nabla}\cdot\boldsymbol{\Sigma}(\delta t, \boldsymbol{W})]\delta t = \boldsymbol{\nabla}\cdot\left[\sqrt{\frac{\eta(k_BT)\delta t}{\Delta V}}(\boldsymbol{W} + \boldsymbol{W}^T)\right],\\
\check{h}(\delta t, \widetilde{\boldsymbol{W}}) &= [\boldsymbol{\nabla}\cdot\boldsymbol{\Psi}(\delta t, \widetilde{\boldsymbol{W}})]\delta t = \boldsymbol{\nabla}\cdot\left[\sqrt{\frac{2\chi\rho\mu_c^{-1}(k_BT)\delta t}{\Delta V}}\widetilde{\boldsymbol{W}}\right],
\end{aligned}$$

where $\widetilde{\boldsymbol{W}}$ and $\boldsymbol{W}$ are vectors of standard Gaussian variables [18].

III-B. ***Higher-order temporal integrators.*** A good strategy for composing higher-order temporal integrators for the low Mach number equations is to use a linear combination of several projected Euler steps of the form (22). In this way, the higher-order integrators inherit the properties of the Euler step. In our case, this will be very useful in constructing conservative discretizations that strictly maintain the EOS constraint and only evaluate fluxes at states that strictly obey the EOS constraint.

The incorporation of stochastic forcing in the Runge–Kutta temporal integrators that we use is described in [29; 18]; here we only summarize the resulting schemes. We note that the stochastic terms should be considered additive noise even though we evaluate them using an instantaneous state like multiplicative noise [73].

Explicit trapezoidal rule. A weakly second-order temporal integrator for (18)–(19) is provided by the *explicit trapezoidal rule*, in which we first take a predictor Euler step

$$\begin{aligned} \boldsymbol{m}^n &= [\mathcal{R}_F^n(\Delta t, \widetilde{\boldsymbol{W}}^n)](\widetilde{\boldsymbol{m}}^n), \\ \rho_1^{\star,n+1} &= \rho_1^n + \Delta t\, \bar{h}^n + \check{h}^n(\Delta t, \widetilde{\boldsymbol{W}}^n), \qquad (23) \\ \widetilde{\boldsymbol{m}}^{\star,n+1} &= \boldsymbol{m}^n + \Delta t\, \bar{\boldsymbol{f}}^n + \check{\boldsymbol{f}}^n(\Delta t, \boldsymbol{W}^n). \qquad (24) \end{aligned}$$

The corrector step is a linear combination of the predictor and another Euler update,

$$\begin{aligned} \boldsymbol{m}^{\star,n+1} &= \big[\mathcal{R}_F^{\star,n+1}(\Delta t, \widetilde{\boldsymbol{W}}^n)\big](\widetilde{\boldsymbol{m}}^{\star,n+1}), \\ \rho_1^{n+1} &= \tfrac{1}{2}\rho_1^n + \tfrac{1}{2}\big[\rho_1^{\star,n+1} + \Delta t\, \bar{h}^{\star,n+1} + \check{h}^{\star,n+1}(\Delta t, \widetilde{\boldsymbol{W}}^n)\big], \qquad (25) \\ \widetilde{\boldsymbol{m}}^{n+1} &= \tfrac{1}{2}\boldsymbol{m}^n + \tfrac{1}{2}\big[\boldsymbol{m}^{\star,n+1} + \Delta t\, \bar{\boldsymbol{f}}^{\star,n+1} + \check{\boldsymbol{f}}^{\star,n+1}(\Delta t, \boldsymbol{W}^n)\big], \qquad (26) \end{aligned}$$

and reuses the same random numbers $\boldsymbol{W}^n$ and $\widetilde{\boldsymbol{W}}^n$ as the predictor step.

Note that both the predicted and the corrected values for density and concentration obey the EOS. We numerically observe that the trapezoidal rule does exhibit a slow but systematic numerical drift in the EOS, and therefore, it is necessary to use the correction procedure described in Section III-C at the end of each time step. The analysis in [18] indicates that for the incompressible case the trapezoidal scheme exhibits second-order weak accuracy in the nonlinear and linearized settings.

Explicit midpoint rule. An alternative second-order scheme is the *explicit midpoint rule*, which can be summarized as follows. First we take a projected Euler step to estimate midpoint values (denoted here with superscript $\star, n+1/2$),

$$\begin{aligned} \boldsymbol{m}^n &= \big[\mathcal{R}_F^n\big(\tfrac{1}{2}\Delta t, \widetilde{\boldsymbol{W}}_1^n\big)\big](\widetilde{\boldsymbol{m}}^n), \\ \rho_1^{\star,n+1/2} &= \rho_1^n + \tfrac{1}{2}\Delta t\, \bar{h}^n + \check{h}^n\big(\tfrac{1}{2}\Delta t, \widetilde{\boldsymbol{W}}_1^n\big), \\ \widetilde{\boldsymbol{m}}^{\star,n+1/2} &= \boldsymbol{m}^n + \tfrac{1}{2}\Delta t\, \bar{\boldsymbol{f}}^n + \check{\boldsymbol{f}}^n\big(\tfrac{1}{2}\Delta t, \boldsymbol{W}_1^n\big), \qquad (27) \end{aligned}$$

and then we complete the time step with another Euler-like update

$$\begin{aligned}
\boldsymbol{m}^{\star,n+1/2} &= \big[\boldsymbol{\mathcal{R}}_F^{n+1/2}(\Delta t,\, \widetilde{\boldsymbol{W}}^n)\big]\big(\widetilde{\boldsymbol{m}}^{\star,n+1/2}\big),\\
\rho_1^{n+1} &= \rho_1^n + \Delta t\, \bar{h}^{\star,n+1/2} + \check{h}^{\star,n+1/2}(\Delta t,\, \widetilde{\boldsymbol{W}}^n),\\
\widetilde{\boldsymbol{m}}^{n+1} &= \boldsymbol{m}^n + \Delta t\, \bar{\boldsymbol{f}}^{\star,n+1/2} + \check{\boldsymbol{f}}^{\star,n+1/2}(\Delta t,\, \boldsymbol{W}^n),
\end{aligned} \tag{28}$$

where the standard Gaussian variates

$$\widetilde{\boldsymbol{W}}^n = \frac{\widetilde{\boldsymbol{W}}_1^n + \widetilde{\boldsymbol{W}}_2^n}{\sqrt{2}}$$

and the vectors of standard normal variates $\widetilde{\boldsymbol{W}}_1^n$ and $\widetilde{\boldsymbol{W}}_2^n$ are independent and similarly for $\boldsymbol{W}_1^n$ and $\boldsymbol{W}_2^n$. Note that $\widetilde{\boldsymbol{W}}_1^n$ and $\boldsymbol{W}_1^n$ are used in *both* the predictor and the corrector stages while $\widetilde{\boldsymbol{W}}_2^n$ and $\boldsymbol{W}_2^n$ are used in the corrector only. Physically, the random numbers $\boldsymbol{W}_1^n/\sqrt{2}$ (and similarly for $\widetilde{\boldsymbol{W}}_1^n$) correspond to the increments of the underlying Wiener processes $\Delta\boldsymbol{\mathcal{B}}_1 = \sqrt{\Delta t/2}\,\boldsymbol{W}_1^n$ over the first half of the time step, and the random numbers $\boldsymbol{W}_2^n/\sqrt{2}$ correspond to the Wiener increments for the second half of the time step [18].

Note that both the midpoint and the endpoint values for density and concentration obey the EOS. We numerically observe that the midpoint rule does not exhibit a systematic numerical drift in the EOS and can therefore be used without the correction procedure described in Section III-C. The analysis in [18] indicates that for the incompressible case the midpoint scheme exhibits second-order weak accuracy in the nonlinear setting. Furthermore, in the linearized setting, it reproduces the steady-state covariances of the fluctuating fields to third order in the time-step size.

Three-stage Runge–Kutta* (*RK3*) *rule. We have also tested and implemented the three-stage Runge–Kutta scheme that was used in [29; 73]. This scheme can be expressed as a linear combination of three Euler steps. The first stage is a predictor Euler step,

$$\boldsymbol{m}^n = [\boldsymbol{\mathcal{R}}_F^n(\Delta t,\, \widetilde{\boldsymbol{W}}^n)](\widetilde{\boldsymbol{m}}^n),$$

$$\rho_1^\star = \rho_1^n + \Delta t\, \bar{h}^n + \check{h}^n(\Delta t,\, \widetilde{\boldsymbol{W}}^n), \tag{29}$$

$$\widetilde{\boldsymbol{m}}^\star = \boldsymbol{m}^n + \Delta t\, \bar{\boldsymbol{f}}^n + \check{\boldsymbol{f}}^n(\Delta t,\, \boldsymbol{W}^n). \tag{30}$$

The second stage is a midpoint predictor

$$\boldsymbol{m}^\star = [\boldsymbol{\mathcal{R}}_F^\star(\Delta t,\, \widetilde{\boldsymbol{W}}^{\star,n})](\widetilde{\boldsymbol{m}}^\star),$$

$$\rho_1^{\star\star} = \tfrac{3}{4}\rho_1^n + \tfrac{1}{4}[\rho_1^\star + \Delta t\, \bar{h}^\star + \check{h}^\star(\Delta t,\, \widetilde{\boldsymbol{W}}^{\star,n})], \tag{31}$$

$$\widetilde{\boldsymbol{m}}^{\star\star} = \tfrac{3}{4}\boldsymbol{m}^n + \tfrac{1}{4}[\boldsymbol{m}^\star + \Delta t\, \bar{\boldsymbol{f}}^\star + \check{\boldsymbol{f}}^\star(\Delta t,\, \boldsymbol{W}^{\star,n})], \tag{32}$$

and a final corrector stage completes the time step

$$\begin{aligned}
\boldsymbol{m}^{\star\star} &= [\mathcal{R}_F^{\star\star}(\Delta t, \widetilde{\boldsymbol{W}}^{\star\star,n})](\widetilde{\boldsymbol{m}}^{\star\star}),\\
\rho_1^{n+1} &= \tfrac{1}{3}\rho_1^n + \tfrac{2}{3}[\rho_1^{\star\star} + \Delta t\, \bar{h}^{\star\star} + \check{h}^{\star\star}(\Delta t, \widetilde{\boldsymbol{W}}^{\star\star,n})], \qquad (33)\\
\widetilde{\boldsymbol{m}}^{n+1} &= \tfrac{1}{3}\boldsymbol{m}^n + \tfrac{2}{3}[\boldsymbol{m}^{\star\star} + \Delta t\, \bar{\boldsymbol{f}}^{\star\star} + \check{\boldsymbol{f}}^{\star\star}(\Delta t, \boldsymbol{W}^{\star\star,n})]. \qquad (34)
\end{aligned}$$

Here the stochastic fluxes between different stages are related to each other via

$$\begin{aligned}
\boldsymbol{W}^n &= \boldsymbol{W}_1^n + \frac{2\sqrt{2}+\sqrt{3}}{5}\boldsymbol{W}_2^n,\\
\boldsymbol{W}^{\star,n} &= \boldsymbol{W}_1^n + \frac{-4\sqrt{2}+3\sqrt{3}}{5}\boldsymbol{W}_2^n,\\
\boldsymbol{W}^{\star\star,n} &= \boldsymbol{W}_1^n + \frac{\sqrt{2}-2\sqrt{3}}{10}\boldsymbol{W}_2^n, \qquad (35)
\end{aligned}$$

where $\boldsymbol{W}_1^n$ and $\boldsymbol{W}_2^n$ are independent and generated independently at each RK3 step (similarly for $\widetilde{\boldsymbol{W}}$). The weights of $\boldsymbol{W}_2^n$ are chosen to maximize the weak order of accuracy of the scheme while still using only two random samples of the stochastic fluxes per time step [18].

The RK3 method is third-order accurate deterministically and stable even in the absence of diffusion/viscosity (i.e., for advection-dominated flows). Note that the predicted, the midpoint, and the endpoint values for density and concentration all obey the EOS. We numerically observe that the RK3 scheme does exhibit a systematic numerical drift in the EOS, and therefore, it is necessary to use the correction procedure described in Section III-C at the end of each time step. The analysis in [18] indicates that for the incompressible case the RK3 scheme exhibits second-order weak accuracy in the nonlinear setting. In the linearized setting, it reproduces the steady-state covariances of the fluctuating fields to third order in the time-step size.

III-C. ***EOS drift.*** While in principle our temporal integrators should strictly maintain the EOS, roundoff errors and the finite tolerance employed in the iterative Poisson solver lead to a small drift in the constraint that can, depending on the specific scheme, lead to an exponentially increasing violation of the EOS over many time steps. In order to maintain the EOS at all times to within roundoff tolerance, we periodically apply a globally conservative L_2 projection of ρ and ρ_1 onto the linear EOS constraint.

This projection step consists of correcting ρ_1 in cell k using

$$(\rho_1)_k \leftarrow A(\rho_1)_k - B(\rho_2)_k - \frac{1}{N}\sum_{k'}[A(\rho_1)_{k'} - B(\rho_2)_{k'}] + \frac{1}{N}\sum_{k'}(\rho_1)_{k'},$$

where N is the number of hydrodynamic cells in the system and

$$A = \frac{\bar{\rho}_1^2}{\bar{\rho}_1^2 + \bar{\rho}_2^2} \quad \text{and} \quad B = \frac{\bar{\rho}_1 \bar{\rho}_2}{\bar{\rho}_1^2 + \bar{\rho}_2^2}.$$

Note that the above update, while nonlocal in nature, conserves the total mass $\sum_{k'} (\rho_1)_{k'}$. A similar update applies to ρ_2, or equivalently, $\rho = \rho_1 + \rho_2$.

IV. Spatial discretization

The spatial discretization we employ follows closely the spatial discretization of the constant-coefficient incompressible equations described in [73]. Therefore, we focus here on the differences, specifically, the use of conserved variables, the handling of the variable-density projection and variable-coefficient diffusion, and the imposition of the low Mach number constraint. Note that the handling of the stochastic momentum and mass fluxes is identical to that described in [73].

For simplicity of notation, we focus on two-dimensional problems with straightforward generalization to three spatial dimensions. Our spatial discretization follows the commonly used MAC approach [43], in which the scalar conserved quantities ρ and ρ_1 are defined on a regular Cartesian grid. The vector conserved variables $\boldsymbol{m} = \rho \boldsymbol{v}$ are defined on a staggered grid such that the k-th component of momentum is defined on the faces of the scalar-variable Cartesian grid in the k-th direction; see Figure 1. For simplicity of notation, we often denote the different components of velocity as $\boldsymbol{v} = (u, v)$ in two dimensions and $\boldsymbol{v} = (u, v, w)$ in three dimensions. The terms "cell-centered", "edge-centered", and "face-centered" refer to spatial locations relative to the underlying scalar grid. Our discretization is based on calculating fluxes on the faces of a finite-volume grid and is thus locally conservative. It is important to note, however, that for the MAC grid different control volumes are used for the scalars and the components of the momentum; see Figure 1.

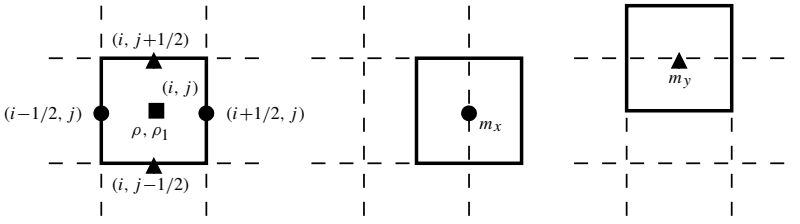

Figure 1. Staggered (MAC) finite-volume discretization on a uniform Cartesian two-dimensional grid. Left: control volume and flux discretization for cell-centered scalar fields such as densities ρ and ρ_1. Middle: control volume for the x-component of face-centered vector fields such as m_x. Right: control volume for the y-component of face-centered vector fields such as m_y.

From the cell-centered ρ and ρ_1, we can define other cell-centered scalar quantities, notably, the concentration $c_{i,j} = (\rho_1)_{i,j}/\rho_{i,j}$ and the transport quantities $\chi_{i,j}$ and $\eta_{i,j}$, which typically depend on the local density $\rho_{i,j}$ and concentration $c_{i,j}$ (and temperature for nonisothermal models) and can, in general, also depend on the spatial position of the cell $(x, y) = (i\Delta x, j\Delta y)$. In order to define velocities, we need to interpret the continuum relationship $\boldsymbol{m} = \rho\boldsymbol{v}$ on the staggered grid. This is done by defining face-centered scalar quantities obtained as an arithmetic average of the corresponding cell-centered quantities in the two neighboring cells. Specifically, we define

$$\rho_{i+1/2,j} = \frac{\rho_{i,j} + \rho_{i+1,j}}{2} \quad \text{and} \quad u_{i+1/2,j} = \frac{(m_x)_{i+1/2,j}}{\rho_{i+1/2,j}}, \tag{36}$$

except at physical boundaries, where the value is obtained from the imposed boundary conditions (see Section IV-E). Arithmetic averaging is only one possible interpolation from cells to faces [2]. In general, other forms of averaging such as a harmonic or geometric average or higher-order, wider stencils [1; 29] can be used. Most components of the spatial discretization can easily be generalized to other choices of interpolation. As we explain later, the use of linear averaging simplifies the construction of conservative advection.

IV-A. ***Diffusion.*** In this section, we describe the spatial discretization of the diffusive mass flux term $\nabla \cdot \rho\chi\nabla c$ in (9). The discretization is based on conservative centered differencing [29; 18]

$$\begin{aligned}(\nabla \cdot \rho\chi\nabla c)_{i,j} = \Delta x^{-1}\Big[\Big(\rho\chi\frac{\partial c}{\partial x}\Big)_{i+1/2,j} - \Big(\rho\chi\frac{\partial c}{\partial x}\Big)_{i-1/2,j}\Big] \\ + \Delta y^{-1}\Big[\Big(\rho\chi\frac{\partial c}{\partial y}\Big)_{i,j+1/2} - \Big(\rho\chi\frac{\partial c}{\partial y}\Big)_{i,j-1/2}\Big],\end{aligned} \tag{37}$$

where, for example,

$$\Big(\rho\chi\frac{\partial c}{\partial x}\Big)_{i+1/2,j} = (\rho_{i+1/2,j})(\chi_{i+1/2,j})\Big(\frac{c_{i+1,j} - c_{i,j}}{\Delta x}\Big) \tag{38}$$

and $\chi_{i+1/2,j}$ is an interpolated face-centered diffusion coefficient, for example, as done for ρ in (36),

$$\chi_{i+1/2,j} = \frac{\chi_{i,j} + \chi_{i+1,j}}{2},$$

except at physical boundaries, where the value is obtained from the imposed boundary conditions.

Regardless of the specific form of the interpolation operator, the same face-centered diffusion coefficient $\chi_{i+1/2,j}$ must be used when calculating the magnitude

of the stochastic mass flux on face $(i+1/2,\, j)$,

$$(\Psi_x)_{i+1/2,\,j} = \sqrt{2\chi_{i+1/2,\,j}(\rho\mu_c^{-1})_{i+1/2,\,j}k_B T}\,\widetilde{\mathcal{W}}_{i+1/2,\,j}.$$

This matches the covariance of the discrete stochastic mass increments $\nabla\cdot\boldsymbol{\Psi}$ with the discretization of the diffusive dissipation operator $\nabla\cdot\rho\chi\nabla$ given in (37)–(38). This matching ensures discrete fluctuation-dissipation balance in the linearized setting [29]. Specifically, at thermodynamic equilibrium, the static covariance of the concentration is determined from the equilibrium value of $(\rho\mu_c^{-1})$ (thermodynamics) independently of the particular values of the transport coefficients (dynamics) as seen in (A-1) and dictated by statistical mechanics principles.

IV-B. ***Viscous terms.*** In [73], a Laplacian form of the viscous term $\eta\boldsymbol{\nabla}^2\boldsymbol{v}$ is assumed, which is not applicable when viscosity is spatially varying and $\boldsymbol{\nabla}\cdot\boldsymbol{v} = S \neq 0$. In two dimensions, the divergence of the viscous stress tensor in the momentum equation (8), neglecting bulk viscosity effects, is

$$\boldsymbol{\nabla}\cdot[\eta(\boldsymbol{\nabla}\boldsymbol{v}+\boldsymbol{\nabla}^T\boldsymbol{v})] = \begin{bmatrix} 2\frac{\partial}{\partial x}(\eta\frac{\partial u}{\partial x}) + \frac{\partial}{\partial y}(\eta\frac{\partial u}{\partial y} + \eta\frac{\partial v}{\partial x}) \\ 2\frac{\partial}{\partial y}(\eta\frac{\partial v}{\partial y}) + \frac{\partial}{\partial x}(\eta\frac{\partial u}{\partial y} + \eta\frac{\partial v}{\partial x}) \end{bmatrix}. \tag{39}$$

The discretization of the viscous terms requires η at cell centers and edges (note that in two dimensions the edges are the same as the nodes $(i+1/2,\, j+1/2)$ of the grid). The value of η at a node is interpolated as the arithmetic average of the four neighboring cell centers,

$$\eta_{i+1/2,\,j+1/2} = \tfrac{1}{4}(\eta_{i,\,j} + \eta_{i+1,\,j+1} + \eta_{i+1,\,j} + \eta_{i,\,j+1}),$$

except at physical boundaries, where the values are obtained from the prescribed boundary conditions. The different viscous friction terms are discretized by straightforward centered differences. Explicitly, for the x-component of momentum,

$$\left[\frac{\partial}{\partial x}\left(\eta\frac{\partial u}{\partial x}\right)\right]_{i+1/2,\,j} = \Delta x^{-1}\left[\left(\eta\frac{\partial u}{\partial x}\right)_{i+1,\,j} - \left(\eta\frac{\partial u}{\partial x}\right)_{i,\,j}\right]$$

with

$$\left(\eta\frac{\partial u}{\partial x}\right)_{i,\,j} = \eta_{i,\,j}\left(\frac{u_{i+1/2,\,j} - u_{i-1/2,\,j}}{\Delta x}\right).$$

Similarly, for the term involving a second derivative in y,

$$\left[\frac{\partial}{\partial y}\left(\eta\frac{\partial u}{\partial y}\right)\right]_{i+1/2,\,j} = \Delta y^{-1}\left[\left(\eta\frac{\partial u}{\partial y}\right)_{i+1/2,\,j+1/2} - \left(\eta\frac{\partial u}{\partial y}\right)_{i+1/2,\,j-1/2}\right]$$

with

$$\left(\eta\frac{\partial u}{\partial y}\right)_{i+1/2,\,j+1/2} = \eta_{i+1/2,\,j+1/2}\left(\frac{u_{i+1/2,\,j+1} - u_{i+1/2,\,j}}{\Delta y}\right).$$

A similar construction is used for the mixed-derivative term

$$\left[\frac{\partial}{\partial y}\left(\eta\frac{\partial v}{\partial x}\right)\right]_{i+1/2,j} = \Delta y^{-1}\left[\left(\eta\frac{\partial v}{\partial x}\right)_{i+1/2,j+1/2} - \left(\eta\frac{\partial v}{\partial x}\right)_{i+1/2,j-1/2}\right]$$

with

$$\left(\eta\frac{\partial v}{\partial x}\right)_{i+1/2,j+1/2} = \eta_{i+1/2,j+1/2}\left(\frac{v_{i+1,j+1/2} - v_{i,j+1/2}}{\Delta x}\right).$$

The stochastic-stress-tensor discretization is described in more detail in [73] and applies in the present context as well. For the low Mach number equations, just as for the compressible equations, the symmetric form of the stochastic stress tensor must be used in order to ensure discrete fluctuation-dissipation balance between the viscous dissipation and stochastic forcing. Additionally, when η is not spatially uniform, the same interpolated viscosity $\eta_{i+1/2,j+1/2}$ as used in the viscous terms must be used when calculating the amplitude in the stochastic forcing $\sqrt{\eta k_B T}$ at the edges (nodes) of the grid.

IV-C. ***Advection.*** It is challenging to construct spatiotemporal discretizations that conserve the total mass while remaining consistent with the equation of state [67; 65; 58] as ensured in the continuum context by the constraint (11). We demonstrate here how the special linear form of the constraint (13) can be exploited in the discrete context. Following [73], we spatially discretize the advective terms in (9) using a centered (skew-adjoint [54]) discretization

$$\begin{aligned}[\nabla\cdot(\rho_1\boldsymbol{v})]_{i,j} &= \Delta x^{-1}[(\rho_1)_{i+1/2,j}u_{i+1/2,j} - (\rho_1)_{i-1/2,j}u_{i-1/2,j}]\\ &\quad + \Delta y^{-1}[(\rho_1)_{i,j+1/2}v_{i,j+1/2} - (\rho_1)_{i,j-1/2}v_{i,j-1/2}]\end{aligned} \tag{40}$$

and similarly for (12). We would like this discrete advection to maintain the equation of state (13) at the discrete level, that is, maintain the constraint relating $(\rho_1)_{i,j}$ and $(\rho_2)_{i,j}$ in every cell (i, j).

Because the different dimensions are decoupled and the divergence is simply the sum of the one-dimensional difference operators, it is sufficient to consider (9) in one spatial dimension. The method-of-lines discretization is given by the system of ODEs, one differential equation per cell i,

$$(\partial_t\rho_1)_i = \Delta x^{-1}(F_{i+1/2} - F_{i-1/2}) - \Delta x^{-1}[(\rho_1)_{i+1/2}u_{i+1/2} - (\rho_1)_{i-1/2}u_{i-1/2}]$$

and similarly for $(\partial_t\rho_2)_i$. As a shorthand, denote the quantity that appears in (13) with

$$\delta = \frac{\rho_1}{\bar\rho_1} + \frac{\rho_2}{\bar\rho_2} = 1.$$

If we use the linear interpolation (36) to calculate face-centered densities, then because of the linearity of the EOS the face-centered densities obey the EOS if the

cell-centered ones do since $\delta_{i+1/2} = (\delta_i + \delta_{i+1})/2 = 1$. The rate of change of δ in cell i is

$$\begin{aligned}\Delta x(\partial_t \delta)_i &= (\rho^{-1}\beta)(F_{i+1/2} - F_{i-1/2}) - [\delta_{i+1/2}u_{i+1/2} - \delta_{i-1/2}u_{i-1/2}] \\ &= (\rho^{-1}\beta)(F_{i+1/2} - F_{i-1/2}) - (u_{i+1/2} - u_{i-1/2}) = 0.\end{aligned}$$

This simple calculation shows that the EOS constraint $\delta = 1$ is obeyed discretely in each cell at all times if it is initially satisfied and the velocities used to advect mass obey the discrete version of the constraint (11),

$$\begin{aligned}S_{i,j} &= \Delta x^{-1}(u_{i+1/2,j} - u_{i-1/2,j}) + \Delta y^{-1}(v_{i,j+1/2} - v_{i,j-1/2}) \\ &= \Big(\frac{1}{\bar\rho_1} - \frac{1}{\bar\rho_2}\Big)\big[\Delta x^{-1}(F_{i+1/2,j} - F_{i-1/2,j}) + \Delta y^{-1}(F_{i,j+1/2} - F_{i,j-1/2})\big],\end{aligned} \tag{41}$$

in two dimensions. Our algorithm ensures that advective terms are always evaluated using a discrete velocity field that obeys this constraint. This is accomplished by using a discrete projection operator as we describe in the next section.

The spatial discretization of the advection terms in the momentum equation (8) is constructed using centered differences on the corresponding shifted (staggered) grid as described in [73]. For example, for the x-component of momentum $m_x = \rho u$,

$$\begin{aligned}[\nabla \cdot (m_x \boldsymbol{v})]_{i+1/2,j} &= \Delta x^{-1}[(m_x u)_{i+1,j} - (m_x u)_{i,j}] \\ &\quad + \Delta y^{-1}[(m_x v)_{i+1/2,j+1/2} - (m_x v)_{i+1/2,j-1/2}],\end{aligned} \tag{42}$$

where simple averaging is used to interpolate momenta to the cell centers and edges (nodes) of the grid, for example,

$$(m_x u)_{i,j} = (m_x)_{i,j} u_{i,j} = \frac{(m_x)_{i-1/2,j} + (m_x)_{i+1/2,j}}{2} \, \frac{u_{i-1/2,j} + u_{i+1/2,j}}{2}. \tag{43}$$

Because of the linearity of the interpolation procedure, the interpolated discrete velocity used to advect m_x obeys the constraint (41) on the shifted grid with a right-hand side $S_{i+1/2,j}$ interpolated using the same arithmetic average used to interpolate the velocities. In particular, in the incompressible case, all variables, including momentum, are advected using a discretely divergence-free velocity, ensuring discrete fluctuation-dissipation balance [73; 18].

It is well-known that the centered discretization of advection we employ here is not robust for advection-dominated flows, and higher-order limiters and upwinding schemes are generally preferred in the deterministic setting [5]. However, these more robust advection schemes add artificial dissipation, which leads to a violation of discrete fluctuation-dissipation balance [18]. In Appendix B, we describe an alternative filtering procedure that can be used to handle strong advection while continuing to use centered differencing.

IV-D. ***Discrete projection.*** We now briefly discuss the spatial discretization of the affine operator $\boldsymbol{\mathcal{R}}_S$ defined by (16) as used in our explicit temporal integrators. The discrete projection takes a face-centered (staggered) discrete velocity field $\tilde{\boldsymbol{v}} = (\tilde{u}, \tilde{v})$ and a velocity divergence S and projects $\boldsymbol{v} = \boldsymbol{\mathcal{R}}_S(\tilde{\boldsymbol{v}})$ onto the constraint (41) in a conservative manner. Specifically, the projection consists of finding a cell-centered discrete scalar field ϕ such that

$$\rho \boldsymbol{v} = \rho \tilde{\boldsymbol{v}} - \nabla \phi \quad \text{and} \quad \nabla \cdot \boldsymbol{v} = S,$$

where the gradient is discretized using centered differences, e.g.,

$$v_{i+1/2,\,j} = \tilde{v}_{i+1/2,\,j} - \left(\frac{1}{\rho_{i+1/2,\,j}}\right)\left(\frac{\phi_{i+1,\,j} - \phi_{i,\,j}}{\Delta x}\right). \tag{44}$$

The pressure correction ϕ is the solution to the variable-coefficient discrete Poisson equation,

$$\begin{aligned} &\frac{1}{\Delta x}\left[\left(\frac{1}{\rho_{i+1/2,\,j}}\right)\left(\frac{\phi_{i+1,\,j} - \phi_{i,\,j}}{\Delta x}\right) - \left(\frac{1}{\rho_{i-1/2,\,j}}\right)\left(\frac{\phi_{i,\,j} - \phi_{i,\,j-1}}{\Delta x}\right)\right] \\ &+ \frac{1}{\Delta y}\left[\left(\frac{1}{\rho_{i,\,j+1/2}}\right)\left(\frac{\phi_{i,\,j+1} - \phi_{i,\,j}}{\Delta y}\right) - \left(\frac{1}{\rho_{i,\,j-1/2}}\right)\left(\frac{\phi_{i,\,j} - \phi_{i,\,j-1}}{\Delta y}\right)\right] \\ &\qquad = S_{i,\,j} - \left[\left(\frac{\tilde{u}_{i+1/2,\,j} - \tilde{u}_{i-1/2,\,j}}{\Delta x}\right) + \left(\frac{\tilde{v}_{i,\,j+1/2} - \tilde{v}_{i,\,j-1/2}}{\Delta y}\right)\right], \end{aligned} \tag{45}$$

which can be solved efficiently using a standard multigrid approach [2].

IV-E. ***Boundary conditions.*** The handling of different types of boundary conditions is relatively straightforward when a staggered grid is used and the physical boundaries are aligned with the cell boundaries for the scalar grid. Interpolation is not used to obtain values for faces, nodes, or edges of the grid that lie on a physical boundary since this would require "ghost" values at cell centers lying outside of the physical domain. Instead, whenever a value of a physical variable is required at a face, node, or edge lying on a physical boundary, the boundary condition is used to obtain that value. Similarly, centered differences for the diffusive and viscous fluxes that require values outside of the physical domain are replaced by one-sided differences that only use values from the interior cell bordering the boundary and boundary values.

For example, if the concentration is specified at the face $(i+1/2,\ j)$, the diffusive flux discretization (38) is replaced with

$$\left(\rho \chi \frac{\partial c}{\partial x}\right)_{i+1/2,\,j} = (\rho_{i+1/2,\,j})(\chi_{i+1/2,\,j})\left(\frac{c_{i+1/2,\,j} - c_{i,\,j}}{\Delta x/2}\right),$$

where $c_{i+1/2,\,j}$ is the specified boundary value, the density $\rho_{i+1/2,\,j}$ is obtained from $c_{i+1/2,\,j}$ using the EOS constraint, and the diffusion coefficient $\chi_{i+1/2,\,j}$ is

calculated at the specified values of concentration and density. Similar straightforward one-sided differencing is used for the viscous fluxes. As discussed in [73], the use of second-order one-sided differencing is not required to achieve global second-order accuracy and would make the handling of the stochastic fluxes more complicated because it leads to a nonsymmetric discrete Laplacian. Note that for the nonlinear low Mach number equations our approach is subtly different from linearly extrapolating the value in the ghost cell $c_{i+1,j} = 2c_{i+1/2,j} - c_i$. Namely, the extrapolated value might be unphysical, and it might not be possible to evaluate the EOS or transport coefficients at the extrapolated concentration. For Neumann-type or zero-flux boundary conditions, the corresponding diffusive flux is set to zero for any faces of the corresponding control volume that lie on physical boundaries, and values in cells outside of the physical domain are never required. The corresponding handling of the stochastic fluxes is discussed in detail in [73].

The evaluation of advective fluxes for the scalars requires normal components of the velocity at the boundary. For faces of the grid that lie on a physical boundary, the normal component of the velocity is determined from the value of the diffusive mass flux at that face using (15). Therefore, these velocities are not independent variables and are not solved for or modified by the projection $\mathcal{R}_S$. Specifically, the discrete pressure ϕ is only defined at the cell centers in the interior of the grid, and the discrete Poisson equation (45) is only imposed on the interior faces of the grid. Therefore, no explicit boundary conditions for ϕ are required when the staggered grid is used, and the natural homogeneous Neumann conditions are implied. Advective momentum fluxes are only evaluated on the interior faces and thus do not use any values outside of the physical domain.

IV-F. ***Summary of Euler–Maruyama method.*** By combining the spatial discretization described above with one of the temporal integrators described in Section III, we can obtain a finite-volume solver for the fluctuating low Mach equations. For the benefit of the reader, here we summarize our implementation of a single Euler step (22). This forms the core procedure that the higher-order Runge–Kutta schemes employ several times during one time step.

(1) Generate the vectors of standard Gaussian variates $\boldsymbol{W}^n$ and $\widetilde{\boldsymbol{W}}^n$.

(2) Calculate diffusive and stochastic fluxes for ρ_1 using (38),

$$\boldsymbol{F}^n = (\rho\chi\nabla c)^n + \boldsymbol{\Psi}^n(\Delta t, \widetilde{\boldsymbol{W}}^n).$$

(3) Solve the Poisson problem (45) with

$$S^n = -\Big(\frac{1}{\bar{\rho}_1} - \frac{1}{\bar{\rho}_2}\Big)\nabla\cdot\boldsymbol{F}^n$$

to obtain the velocity $\boldsymbol{v}^n$ from $\tilde{\boldsymbol{v}}^n = \widetilde{\boldsymbol{m}}^n/\rho^n$ using (44), enforcing $\nabla\cdot\boldsymbol{v}^n = S^n$.

(4) Calculate viscous and stochastic momentum fluxes using (39),

$$\nabla \cdot [\eta(\nabla \boldsymbol{v} + \nabla^T \boldsymbol{v})]^n + \nabla \cdot [\boldsymbol{\Sigma}^n(\Delta t, \boldsymbol{W}^n)].$$

(5) Calculate external forcing terms for the momentum equation such as the contribution $-\rho^n \boldsymbol{g}$ due to gravity.

(6) Calculate advective fluxes for mass and momentum using (40) and (42).

(7) Update mass and momentum densities, including advective, diffusive, stochastic, and external forcing terms, to obtain ρ^{n+1}, ρ_1^{n+1}, and $\widetilde{\boldsymbol{m}}^{n+1}$. Note that this update preserves the EOS constraint as explained in Section IV-C.

We have tested and validated the accuracy of our methods and numerical implementation using a series of standard deterministic tests as well as by examining the equilibrium spectrum of the concentration and velocity fluctuations [29; 73; 18]. The next two sections present further verification and validation in the context of nonequilibrium systems.

V. Giant concentration fluctuations

Advection of concentration by thermal velocity fluctuations in the presence of large concentration gradients leads to the appearance of *giant fluctuations* of concentration, as has been studied theoretically and experimentally for more than a decade [77; 12; 75; 74]. These giant fluctuations were previously simulated in the absence of gravity in three dimensions by some of us in [73], and good agreement was found with experimental results [75]. In those previous studies, the incompressible equations were used; that is, it was assumed that concentration was a passively advected scalar. However, it is more physically realistic to account for the fact that the properties of the fluid, notably the density and the transport coefficients, depend on the concentration. In [12], a series of experiments were performed to study the temporal evolution of giant concentration fluctuations during the diffusive mixing of water and glycerol, starting with a glycerol mass fraction of $c = 0.39$ in the bottom half of the experimental domain and $c = 0$ in the top half. Because it is essentially impossible to analytically solve the full system of fluctuating equations in the presence of spatial inhomogeneity and nontrivial boundary conditions, the existing theoretical analysis of the diffusive mixing process [77] makes a quasiperiodic constant-coefficient incompressible approximation.

For simplicity, in this section, we focus on a time-independent problem and study the spectrum of steady-state concentration fluctuations in a mixture under gravity in the presence of a constant concentration gradient. This extends the study reported in [73] to account for the fact that the density, viscosity, and diffusion coefficient depend on the concentration. For simplicity, we do two-dimensional simulations since for this problem there is no difference between the spectra of

concentration fluctuations in two and three dimensions [73] (note, however, that in real space, unlike in Fourier space, the effect of the fluctuations on the transport is very different in two and three dimensions). Furthermore, in these simulations, we do not include a stochastic flux in the concentration equation; i.e., we set $\mathbf{\Psi} = 0$ so that all fluctuations in the concentration arise from being out of thermodynamic equilibrium. With this approximation, we do not need to model the chemical potential of the mixture and obtain μ_c. This formulation is justified by the fact that it is known experimentally that the nonequilibrium fluctuations are much larger than the equilibrium ones for the conditions we consider [12].

In the simple linearized theory presented in Section A.2, several approximations are made. The first one is that a quasiperiodic approximation is used even though the actual system is not periodic in the y-direction. This source of error has already been studied numerically in [73]. We also use a Boussinesq approximation where it is assumed that $\bar{\rho}_1 = \rho_0 + \Delta\rho/2$ and $\bar{\rho}_2 = \rho_0 - \Delta\rho/2$, where $\Delta\rho$ is a small density difference between the two fluids, $\Delta\rho/\rho_0 \ll 1$, so that density is approximately constant and $\beta \ll 1$. More precisely, in the Boussinesq model, the gravity term in the velocity equation only enters through the product βg, so the approximation consists of taking the limit $\beta \to 0$ and $g \to \infty$ while keeping the product βg fixed. The final approximation made in the simple theory is that the transport coefficients, i.e., the viscosity and diffusion coefficients, are assumed to be constant. Here we evaluate the validity of the constant-coefficient constant-density approximation (ρ, η, and χ constant and $\beta \to 0$), as well as the constant-density (Boussinesq) approximation alone (ρ constant and $\beta \to 0$ but variable η and χ), by comparing with the solution to the complete low Mach number equations (ρ, η, χ, and β variable).

V-A. ***Simulation parameters.*** We base our parameters on the experimental studies of diffusive mixing in a water-glycerol mixture as reported in [12]. The physical domain is $1\text{ cm} \times 0.25\text{ cm}$ discretized on a uniform 128×32 two-dimensional grid with a thickness of 1 cm along the z-direction. Gravity is applied in the negative y- (vertical) direction. Reservoir boundary conditions (15) are applied in the y-direction and periodic boundary conditions in the x-direction. We set the concentration to $c = 0.39$ on the bottom boundary and $c = 0$ on the top boundary and apply no-slip boundary conditions for the velocity at both boundaries. The initial condition is $c(t = 0) = 0.39(y/0.25 - 1)$, which is close to the deterministic steady-state profile. A very good fit to the experimental equation of state (dependence of density on concentration at standard temperature and pressure) over the whole range of concentrations of interest is provided by the EOS (13) with the density of water set to $\bar{\rho}_2 = 1\text{ g/cm}^3$ and the density of glycerol set to $\bar{\rho}_1 = 1.29\text{ g/cm}^3$. In these simulations, the magnitude of the velocity fluctuations is very small, and we did not use filtering (see Appendix B).

Experimentally, the dependence of viscosity on glycerol mass fraction has been fit to an exponential function [12], which we approximate with a quadratic function over the range of concentrations of interest

$$\eta(c) = \rho(c)\nu(c) = \rho_0\nu_0 \exp(2.06c + 2.32c^2) \approx \rho_0\nu_0(1.0 + 0.66c + 12c^2), \quad (46)$$

where $\rho_0 = 1\,\mathrm{g/cm^3}$ and experimental measurements estimate $\nu_0 \approx 10^{-2}\,\mathrm{cm^2/s}$. The dependence of the diffusion coefficient on the concentration has been studied experimentally [19], but it is strongly affected by thermal fluctuations and spatial confinement [24; 21; 26]. We approximate the dependence assuming a Stokes–Einstein relation [25], which is in reasonable agreement with the experimental results in [19] over the range of concentrations of interest here; we can write it as

$$\chi(c) = \frac{\chi_0\eta_0}{\eta(c)} \approx \chi_0(1.0 - 2.2c + 1.2c^2), \quad (47)$$

where experimental estimates for water-glycerol mixtures give $\chi_0 \approx 10^{-5}\,\mathrm{cm^2/s}$, with a Schmidt number $\mathrm{Sc} = \nu_0/\chi_0 \approx 10^3$. This very large separation of scales between mass and momentum diffusion is not feasible to simulate with our explicit temporal integration methods. Referring back to the simplified theory (A-7), which in this case can be simplified further to

$$S_{c,c}(k_x, k_y = 0) = \left\langle (\widehat{\delta c})(\widehat{\delta c})^\star \right\rangle \approx \frac{\nu}{\nu + \chi} \frac{k_B T}{\left(\chi\eta k_x^4 + h_\parallel \rho g \beta\right)} h_\parallel^2, \quad (48)$$

we see that for $\nu \gg \chi$ the shape of the spectrum of the steady-state concentration fluctuations, and in particular the cutoff wavenumber due to gravity, is determined from the product $\chi\nu$ and not χ and ν individually. Therefore, as also done in [73], we choose χ_0 and ν_0 so that $\chi(\bar{c})\nu(\bar{c})$ is kept at the physical value of $10^{-7}\,\mathrm{g\cdot cm/s^2}$, but the Schmidt number is reduced by two orders of magnitude, $S_c = \rho_0^{-1}\eta(\bar{c})/\chi(\bar{c}) = 10$, where $\bar{c} = 0.39/2$ is an estimate of the average concentration. The condition $\eta(\bar{c}) \approx 10^{-3}\,\mathrm{g/(cm\cdot s)}$ and $\chi(\bar{c}) \approx 10^{-4}\,\mathrm{cm^2/s}$ gives our simulation parameters $\nu_0 \approx 6.1 \times 10^{-4}\,\mathrm{cm^2/s}$ and $\chi_0 \approx 1.6 \times 10^{-4}\,\mathrm{cm^2/s}$.

The physical value for gravity is $g \approx 10^3\,\mathrm{cm/s^2}$, and the solutal expansion coefficient $\beta(\bar{c}) \approx 0.234$ follows from $\bar{\rho}_1$ and $\bar{\rho}_2$. When employing the Boussinesq approximation, in which gravity only enters through the product βg, we set $\rho_1 = 1.054$ and $\rho_2 = 1.044$ so that $\beta = 0.01$ and increase gravity by the corresponding factor to $g = 2.34 \cdot 10^4\,\mathrm{cm/s^2}$ in order to keep βg fixed at the physical value. We also performed simulations with a weaker gravity, $g \approx 10^2\,\mathrm{cm/s^2}$, which enhances the giant fluctuations.

V-B. ***Results.*** We employ the explicit midpoint temporal integrator (which we recall is third-order accurate for static covariances) and set $\Delta t = 0.005\,\mathrm{s}$, which results in a diffusive Courant number $\nu\Delta t/\Delta x^2 \approx 0.1$. We skip the first 50,000

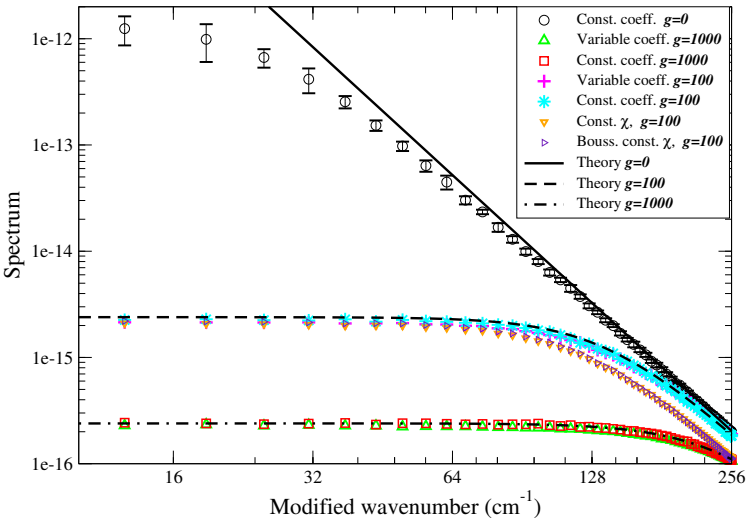

Figure 2. Comparison between the simple theory (A-7) (lines) and numerical results (symbols). Results are shown for standard gravity $g \approx 10^3\,\mathrm{cm/s^2}$ (the cutoff wavenumber $k_g \approx 246\,\mathrm{cm}^{-1}$) for the complete variable-coefficient variable-density low Mach model (green upward triangles) and the constant-coefficient constant-density approximation (red squares). Also shown are results for a weaker gravity, $g \approx 10^2\,\mathrm{cm/s^2}$ (the cutoff wavenumber $k_g \approx 138\,\mathrm{cm}^{-1}$), for the complete low Mach model (magenta pluses) and the constant-coefficient constant-density approximation (cyan stars). For comparison, results for $g \approx 10^2\,\mathrm{cm/s^2}$ with variable viscosity $\eta(c)$ but constant diffusion coefficient $\chi(c) = \chi_0$ are also shown, for variable density (orange downward triangles) and the constant-density (Boussinesq) approximation (indigo right-facing triangles). Finally, results for no gravity are shown in the constant-coefficient approximation (black circles).

time steps (about five diffusion crossing times) and then collect samples from the subsequent 50,000 time steps. We repeat this eight times to increase the statistical accuracy and estimate error bars. To compare to the theory (A-7), we set the concentration gradient to $h_\parallel = 0.39/0.25\,\mathrm{cm}^{-1}$ and evaluate $\rho \approx 1.05\,\mathrm{g/cm^3}$ at $c = 0.39/2$ from the equation of state. When computing the theory, we account for errors in the discrete approximation to the continuum Laplacian by using the effective wavenumber

$$k_\perp = k_x \frac{\sin(k_x \Delta x/2)}{(k_x \Delta x/2)} \tag{49}$$

instead of the actual discrete wavenumber k_x [73].

The results for the static spectrum of concentration fluctuations $S_{c,c}(k_x, k_y = 0) = \langle(\widehat{\delta c})(\widehat{\delta c})^\star\rangle$ as a function of the modified wavenumber $k_\perp$ (49) are shown in Figure 2. When there is no gravity, we see the characteristic giant-fluctuation power-law spectrum of the fluctuations, modulated at small wavenumbers due to the presence of the physical boundaries [73]. When gravity is present, fluctuations at wavenumber

below the cutoff $k_g = [h_\parallel \rho g \beta/(\eta\chi)]^{1/4}$ are suppressed. If we use a constant-coefficient approximation, in which we reduce $\beta = 0.01$ so that $\rho \approx \rho(\bar{c})$ and also fix the transport coefficients at $\eta(c) = \eta(\bar{c})$ and $\chi(c) = \chi(\bar{c})$, we observe good agreement with the quasiperiodic theory (A-7). When we make the transport coefficients dependent on the concentration as in (46) and (47), we observe a rather small change in the spectrum. This is perhaps not unexpected because the simplified theory (48) shows that only the product $\chi\eta$, and not χ and η individually, matters. Since we used the Stokes–Einstein relation $\chi(c)\eta(c) = \rho_0\chi_0\nu_0 =$ constant to select the concentration dependence of the diffusion coefficient, the value of $\chi\eta$ is constant throughout the physical domain. For comparison, in Figure 2 we show results from a simulation where we keep the concentration dependence of the viscosity (46) but set the diffusion coefficient to a constant value, $\chi(c) = \chi_0$, and we observe a more significant change in the spectrum. Further employing the Boussinesq approximation makes little difference, showing that the primary effect here comes from the dependence of the transport coefficients on concentration.

This shows that, under the sort of parameters present in the experiments on diffusive mixing in water-glycerol mixture, it is reasonable to make the Boussinesq incompressible approximation; however, the spatial dependence of the viscosity and diffusion coefficient cannot in general be ignored if quantitative agreement is desired. In particular, time-dependent quantities such as dynamic spectra [76; 11] depend on the values of χ and η and not just their product, and are thus expected to be more sensitive to the details of their concentration dependence. Even though the constant-coefficient approximation gives qualitatively the correct shape and a better choice of the constant transport coefficients may improve its accuracy, there is no simple procedure to a priori estimate what parameters should be used (but see [77] for a proposal to average the constant-coefficient theory over the domain). A direct comparison with experimental results is not possible until multiscale temporal integrators capable of handling the extreme separation of time scales between mass and momentum diffusion are developed. At present, this has only been accomplished in the constant-coefficient incompressible limit ($\beta = 0$) [26], and it remains a significant challenge to accomplish the same for the complete low Mach number system.

VI. Diffusive mixing in hard-disk and hard-sphere fluids

In this section, we study the appearance of giant fluctuations during *time-dependent* diffusive mixing. As a validation of the low Mach number fluctuating equations and our algorithm, we perform simulations of diffusive mixing of two fluids of different densities in two dimensions. We find excellent agreement between the results of low Mach number (continuum) simulations and hard-disk molecular dynamics (particle)

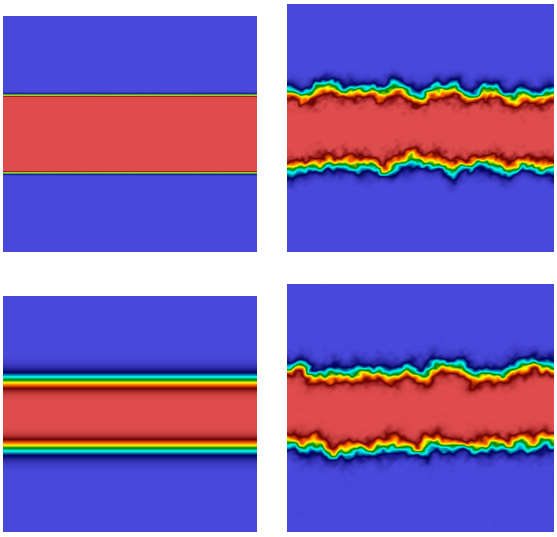

Figure 3. Diffusive mixing between two fluids of unequal densities, $R = \rho_2/\rho_1 = 4$, with coloring based on concentration: red for the pure first component, $c = 1$, and blue for the pure second component, $c = 0$. A smoothed shading is used for the coloring to eliminate visual discretization artifacts. The simulation domain is periodic and contains 128^2 hydrodynamic (finite-volume) cells. The top left panel shows the initial configuration, which is the same for all simulations reported here. The top right panel shows the final configuration at time $t = 5800$ as obtained using molecular dynamics. The bottom left panel shows the final configuration obtained using deterministic hydrodynamics while the bottom right panel shows the final configuration obtained using fluctuating hydrodynamics.

simulations. This nontrivial test clearly demonstrates the usefulness of low Mach number models as a coarse-grained mesoscopic model for problems where sound waves can be neglected.

Our simulation setup is illustrated in Figure 3. We consider a periodic square box of length L along both the x- (horizontal) and y- (vertical) directions and initially place all of the fluid of species one (colored red) in the middle third of the domain; i.e., we set $c = 1$ for $L/3 \le y \le 2L/3$, and $c = 0$ otherwise, as shown in the top left panel of the figure. The two fluids mix diffusively, and at the end of the simulation, the concentration field shows a *rough diffusive interface* as confirmed by molecular dynamics simulations shown in the top right panel of the figure. The deterministic equations of diffusive mixing reduce to a one-dimensional model due to the translational symmetry along the x-axis and would yield a *flat* diffusive interface as illustrated in the bottom left panel of the figure. However, fluctuating hydrodynamics correctly reproduces the interface roughness as illustrated in the bottom right panel of the figure and demonstrated quantitatively below.

We consider here a binary hard-disk mixture in two dimensions. We use arbitrary (molecular) units of length, time, and mass for convenience. All hard disks had

a diameter $\sigma = 1$ in arbitrary units, and we set the temperature at $k_B T = 1$. The molecular mass for the first fluid component was fixed at $m_1 = 1$ and for the second component at $m_2 = Rm_1$. For mass ratio $R = 1$, the two types of disks are mechanically identical, and therefore, the species label is simply a red-blue coloring of the particles. In this case, $\bar{\rho}_2 = \bar{\rho}_1$ and the low Mach number equations reduce to the incompressible equations of fluctuating hydrodynamics with a passively advected concentration field. For the case of unequal particle masses, mechanical equilibrium is obtained if the pressures in the two fluid components are the same. It is well-known from statistical mechanics that for hard disks or hard spheres the pressure is

$$P = Y(\phi) \cdot n \cdot k_B T,$$

where $n = N/V$ is the number density and $Y(\phi)$ is a prefactor that only depends on the packing fraction $\phi = n(\pi\sigma^2/4)$ and not on the molecular mass. Therefore, for a mixture of disks or spheres with equal diameters, at constant pressure, the number density and the packing fraction ϕ are constant independent of the composition. The equation of state at constant pressure and temperature is therefore

$$1 = \frac{n_1}{n} + \frac{n_2}{n} = \frac{\rho_1}{nm_1} + \frac{\rho_2}{nm_2},$$

which is exactly of the form (13) with $\bar{\rho}_1 = nm_1$ and $\bar{\rho}_2 = nm_2$. The chemical potential of such a mixture has the same concentration dependence as a low-density gas mixture [49],

$$\mu_c^{-1} k_B T = c(1-c)[cm_2 + (1-c)m_1].$$

VI-A. ***Hard-disk molecular dynamics.*** In order to validate the predictions of our low Mach number model, we performed hard-disk molecular dynamics (HDMD) simulations of diffusive mixing using a modification of the public-domain code developed by the authors of [70]. We used a packing fraction of $\phi = 0.6$ for all simulations reported here. This packing fraction is close to the freezing transition point but is known to be safely in the (dense) gas phase (there is no liquid phase for a hard-disk fluid). The initial particle positions were generated using a nonequilibrium molecular-dynamics simulation as in the hard-particle packing algorithm described in [27; 28]. After the initial configuration was generated, the disks were assigned a species according to their y-coordinate, and the mixing simulation was performed using event-driven molecular dynamics.

In order to convert the particle data to hydrodynamic data comparable to that generated by the fluctuating hydrodynamics simulations, we employed a grid of N_c^2 hydrodynamic cells that were each a square of linear dimension $L_c = 10\sigma$. At the chosen packing fraction $\phi = 0.6$, this corresponds to about 76 disks per hydrodynamic cell, which is deemed a reasonable level of coarse-graining for the equations

of fluctuating hydrodynamics to be a reasonably accurate model while still keeping the computational demands of the simulations manageable. We performed HDMD simulations for systems of size $N_c = 64$ and $N_c = 128$ cells and simulated the mixing process to a final simulation time of $t = 5800$ units. The largest system simulated had about 1.25 million disks (each simulation took about five days of CPU time), which is well into the "hydrodynamic" rather than "molecular" scale.

Every 58 units of time, particle data was converted to hydrodynamic data for the purposes of analysis and comparison to hydrodynamic calculations. There is not a unique way of coarse-graining particle data to hydrodynamic data [78; 35]; however, we believe that the large-scale (giant) concentration fluctuations studied here are *not* affected by the particular choice. We therefore used a simple method consistent with the philosophy of finite-volume conservative discretizations. Specifically, we coarse-grained the particle information by sorting the particles into hydrodynamic cells based on the position of their centroid as if they were point particles. We then calculated ρ_1 and ρ_2 in each cell based on the total mass of each species contained inside the given cell. Since all particles have equal diameter, other definitions that take into account the particle shape and size give similar results.

VI-B. ***Hard-disk hydrodynamics.*** We now turn to hydrodynamic simulations of the diffusive mixing of hard disks. Our hydrodynamic calculations use the same grid of cells used to convert particle to hydrodynamic data. The only input required for the hydrodynamic calculations, in addition to those provided by equilibrium statistical mechanics, are the transport coefficients of the fluid as a function of concentration, specifically, the shear viscosity η and the diffusion coefficient χ.

The values for the transport coefficients used in the spatiotemporal discretization, as explained in [24; 26] and detailed in Appendix C, are not material constants independent of the discretization. Rather, they are *bare* transport values η_0 and χ_0 measured at the length scales of the grid size. We assumed that the bare transport coefficients obey the same scaling with the mass ratio R as predicted by Enskog kinetic theory (C-1)–(C-2). As explained in Appendix C, theoretical arguments and molecular-dynamics results suggest that renormalization effects for viscosity are small and can be safely neglected. We have therefore fixed the viscosity in the hydrodynamic calculations based on the molecular-dynamics estimate $\eta_0 = 2.5$ for the pure fluid with molecular mass $m = 1$ (see Section C.1). However, the bare diffusion coefficient is strongly dependent on the size of the hydrodynamic cells (held fixed in our calculations at $\Delta x = \Delta y = 10$) and on whether filtering (see Appendix B) is used. Therefore, the value of χ_0 needs to be adjusted based on the spatial discretization in such a way as to match the behavior of the molecular-dynamics simulations at length scales much larger than the grid spacing. We describe the exact procedure we used to accomplish this in Section C.2.

The time step in our explicit algorithm is limited by the viscous CFL number $\alpha_\nu = \nu\Delta t/\Delta x^2 < 1/4$. Since the hydrodynamic calculations are much faster compared to the particle simulations, we used the more expensive RK3 temporal integrator with a relatively small time step $\Delta t = 1.45$, corresponding to $\alpha_\nu \approx 0.05$ for $c = 1$. For $R = 1$ and $N_c = 64$, we employed a larger time step, $\Delta t = 3.625$ ($\alpha_\nu \approx 0.125$), with no measurable temporal discretization artifacts for the quantities studied here. We are therefore confident that the discretization errors in this study are dominated by spatial discretization artifacts. In future work, we will explore semi-implicit discretizations and study the effect of taking larger time steps on temporal accuracy. Note that at these parameters for $c = 1$ the isothermal speed of sound is $c_T \approx 5.1$ so that a compressible scheme would require a time step on the order of $\Delta t \sim 1$ (corresponding to advective CFL of about $1/2$). By contrast, the explicit low Mach number algorithm is stable for $\Delta t \lesssim 7.5$. This modest gain is due to the small hydrodynamic cell we use here in order to compare to molecular dynamics. For mesoscopic hydrodynamic cells, the gain in time-step size afforded by the low Mach formulation will be several orders of magnitude larger.

For mass ratio $R = 1$ and $R = 2$, the hydrodynamic calculations were initialized using statistically identical configurations as would be obtained by coarse-graining the initial particle configuration. This implies a sharp, step-like jump in concentration at $y = L/3$ and $y = 2L/3$. Since our spatiotemporal discretization is not strictly monotonicity-preserving, such sharp concentration gradients combined with a small diffusion coefficient χ_0 lead to a large cell Peclet number. This may in turn lead to large deviations of concentration outside of the allowed interval $0 \le c \le 1$ for larger mass ratios. Therefore, for $R = 4$, we smoothed the initial condition slightly so that the sharp jump in concentration is spread over a few cells and also employed a nine-point filter for the advection velocity ($w_F = 4$; see Appendix B). We verified that for $R = 2$ using filtering only affects the large wavenumbers and does not appear to affect the small wavenumbers we study here, provided the bare diffusion coefficient χ_0 is adjusted based on the specific filtering width w_F.

VI-C. ***Comparison between molecular-dynamics and fluctuating hydrodynamics simulations.*** In order to compare the molecular-dynamics and the hydrodynamic simulations, we calculated several statistical quantities:

(1) The averages of ρ_1 along the directions perpendicular to the concentration gradient,

$$\rho_1^{(h)}(y) = L^{-1} \int_{x=0}^{L} \rho_1(x, y)\, dx, \tag{50}$$

where the integral is discretized as a direct sum over the hydrodynamic cells. Note that it is statistically better to use conserved quantities for such macroscopic averages than to use nonconserved variables such as concentration [37].

(2) The spectrum of the concentration averaged along the direction of the gradient by computing the average

$$c_v(x) = L^{-1} \int_{y=0}^{L} c(x, y)\, dy$$

and then taking the discrete Fourier transform. Intuitively, c_v is a measure of the thickness of the red strip in Figure 3 and corresponds closely to what is measured in light-scattering and shadowgraphy experiments [61; 12].

(3) The discrete Fourier spectrum of the y-coordinate of the "center of mass" of concentration along the direction perpendicular to the gradient,

$$h_c(x) = L^{-1} \int_{y=0}^{L} y \cdot c(x, y)\, dy.$$

Intuitively, h_c is a measure of the height of the centerline of the red strip in Figure 3.

All quantities were sampled at certain prespecified time points in a number of statistically independent simulations N_s and then means and standard deviations calculated from the N_s data points. For systems of size $N_c = 64$ cells, we used $N_s = 64$ simulations, and for systems of size $N_c = 128$, we used $N_s = 32$ simulations. By far the majority of the computational cost was in performing the HDMD simulations.

Average concentration profiles. Once χ_0 and χ_{eff} were estimated based on simulations of a constant-density ($R = 1$) fluid (see Section C.2), kinetic theory, i.e., Equations (C-1) and (C-2), can be used to estimate them for different density ratios. In Figure 9 (page 99), we show $\rho_1^{(h)}(y)$ for mass ratio $R = 2$, showing good agreement between HDMD and hydrodynamics especially when fluctuations are accounted for. For $R = 4$, a direct comparison is difficult because the initial condition was slightly different in the hydrodynamic simulations due to the need to smooth the sharp concentration gradient for numerical reasons as explained earlier. This difference strongly affects the shape of $\rho_1^{(h)}(y)$ at early times; however, it does not significantly modify the roughness of the interface, which we study next.

Interface roughness. The most interesting contribution of fluctuations to the diffusive mixing process is the appearance of giant concentration fluctuations in the presence of large concentration gradients as evidenced in the roughness of the interface between the two fluids during the early stages of the mixing in Figure 3. In order to quantify this interface roughness, we used the one-dimensional power spectra

$$S_c(k_x) = \langle \hat{c}_v \hat{c}_v^{\star} \rangle \quad \text{and} \quad S_h(k_x) = \langle \hat{h}_c \hat{h}_c^{\star} \rangle.$$

Note that here we do not correct the discrete wavenumber for the spatial discretization artifacts and continue to use k_x instead of $k_\perp$.

The temporal evolution of the spectra S_c and S_h is shown in Figure 4 for mass

ratio $R = 1$, and in Figure 5 for mass ratio $R = 4$, for both HDMD and low Mach number fluctuating hydrodynamics (note that deterministic hydrodynamics would give identically zero for any spectral quantity). We observe an excellent agreement between the two, including the correct initial evolution of the interface fluctuations.

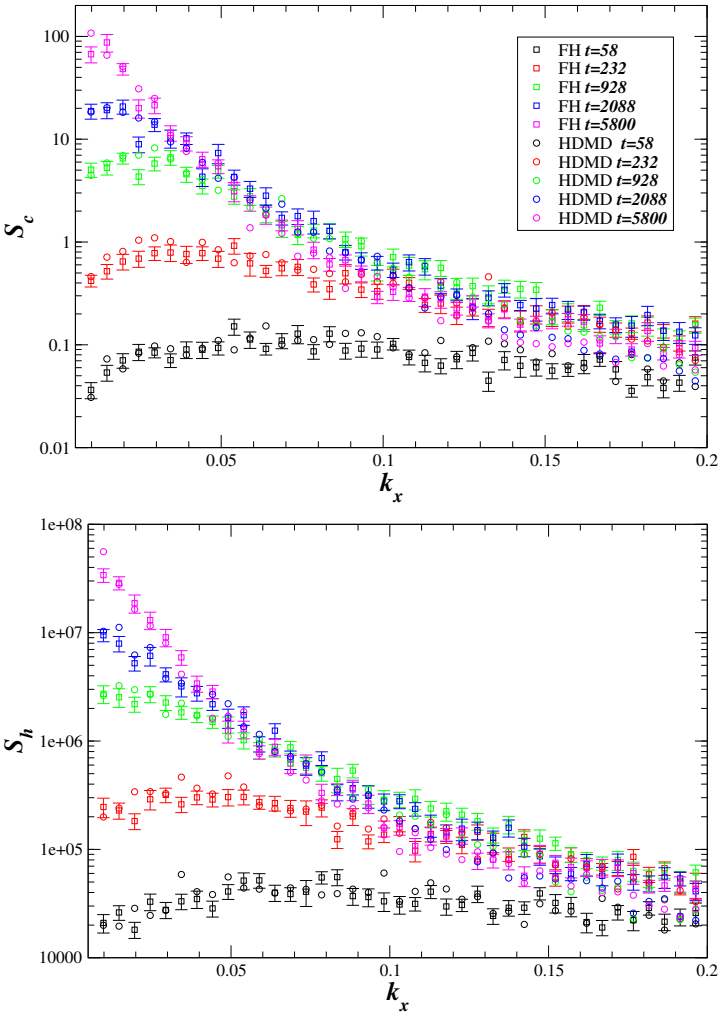

Figure 4. Discrete spatial spectrum of the interface fluctuations for $R = 1$ and $N_c = 128$ (averaged over 32 simulations) at several points in time (drawn with different colors as indicated in the legend) for fluctuating hydrodynamics (FH, squares with error bars) and HDMD (circles, error bars comparable to those for squares). Note that the largest wavenumber supported by the grid is $k_{\max} = \pi/\Delta x \approx 0.314$. The larger wavenumbers are however dominated by spatial truncation errors and the filter employed (if any), and we do not show them here. Top: spectrum $S_c(k_x)$ of the vertically averaged concentration. Bottom: spectrum $S_h(k_x)$ of the position of the vertical "center of mass" of concentration.

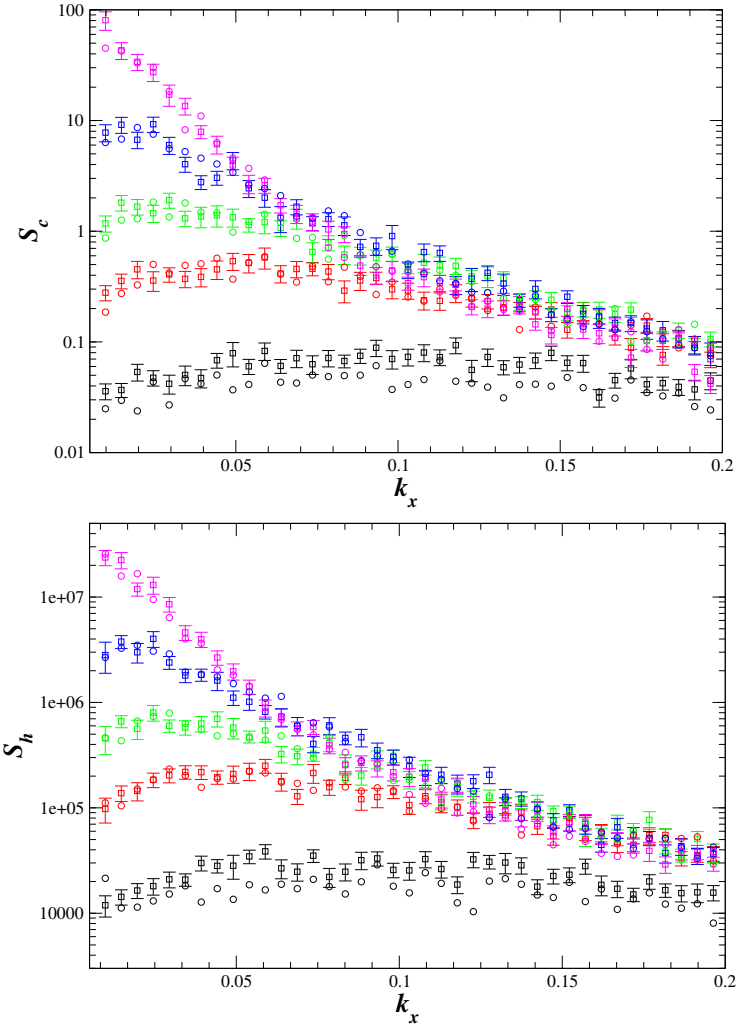

Figure 5. Same as Figure 4 but for density ratio $R = 4$.

Note that, for a finite system, eventually complete mixing will take place and the concentration fluctuations will have to revert to their equilibrium spectrum, which is flat in Fourier space instead of the power-law behavior seen out of equilibrium. In Figure 6, we show results for mixing up to a time $t = 7.42 \cdot 10^5$ (this is 128 times longer than those described above). These long simulations are only feasible for the fluctuating hydrodynamics code and employ a somewhat larger time step $\Delta t = 3.625$. The results clearly show that at late times the spectrum of the fluctuations reverts to the equilibrium one; however, this takes some time even after the mixing is essentially complete. Linearized incompressible fluctuating hydrodynamics [77; 73] predicts that at steady state the spectrum of nonequilibrium concentration

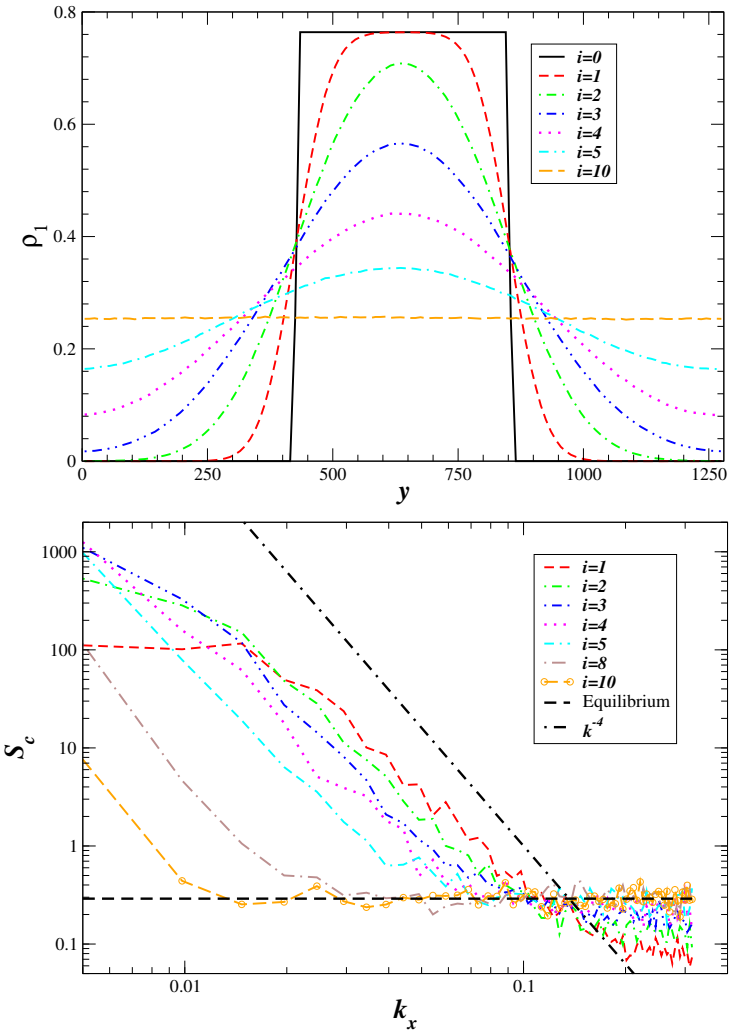

Figure 6. Mixing to a time 128 times longer than previous results with results reported at time intervals $t = 7424\, i^2$ for $i = 1, \ldots, 10$. These long simulations are only feasible for the fluctuating hydrodynamics code and employ a somewhat larger time step $\Delta t = 3.625$. Top: horizontally averaged ρ_1 as shown for the shorter runs in the top panel of Figure 9. Bottom: the spectrum of interface fluctuations $S_c(k_x)$ as shown in the top panels of Figures 4 and 5 for the shorter runs. The theoretical estimates for the spectrum of equilibrium fluctuations, which is independent of wavenumber, is also shown. We also indicate the theoretical prediction for the power law of the spectrum of steady-state nonequilibrium fluctuations under an applied concentration gradient, $S_c \sim k^{-4}$.

fluctuations is a power law with exponent -4, $S_c \sim (\nabla c)^2 k^{-4}$. The dynamically evolving spectra in the bottom panel of Figure 6 show approximately such power-law behavior for intermediate times and wavenumbers.

VI-D. ***Hard-sphere fluctuating hydrodynamics simulations.*** In order to illustrate the appearance of giant fluctuations in three dimensions, we performed simulations of mixing in a mixture of hard spheres with equal diameters, $\sigma = 1$, and mass ratio $R = 4$. The packing density was chosen to be $\phi = 0.45$, which corresponds to a very dense gas but is still well below the freezing point $\phi_f = 0.49$. For the hydrodynamic simulations, we used cubic cells of dimension $\Delta x = 5$, which corresponds to about 107 particles per hydrodynamic cell on average. In Figure 7, we show results from a single simulation with a grid of size $128 \times 64 \times 128$ cells, which would correspond to about 10^8 particles. This makes molecular-dynamics simulations infeasible and makes hydrodynamic calculations an invaluable tool in studying the mixing process at these mesoscopic scales.

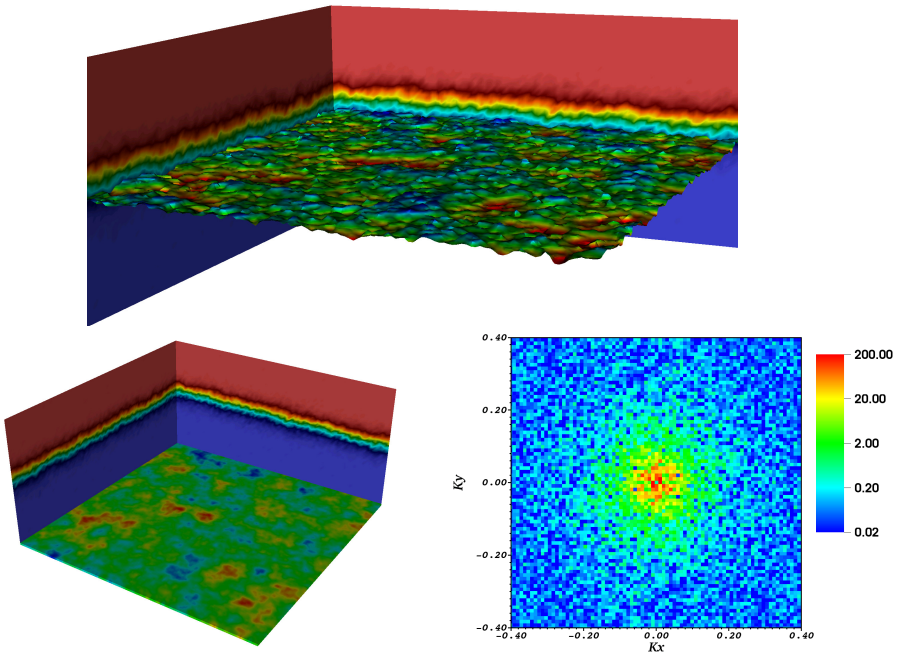

Figure 7. Diffusive mixing in three dimensions similar to that illustrated in Figure 3 for two dimensions. Parameters are based on Enskog kinetic theory for a hard-sphere fluid at packing fraction $\phi = 0.45$, and there is no gravity. The mixing starts with the top half being one species and the bottom half another species with density ratio $R = 4$, and concentration is kept fixed at the top and bottom boundaries while the side boundaries are periodic. A snapshot taken at time $t = 5000$ is shown. Top: the side panes show two-dimensional slices for the concentration c. The approximated contour surface $c = 0.2$ is shown with color based on surface height to illustrate the rough diffusive interface. Bottom left: similar to top panel, but bottom pane shows vertically averaged concentration $c_v(x, z)$, illustrating the giant concentration fluctuations. Bottom right: the Fourier spectrum $S_c(k_x, k_y)$ of c_v. The color axis is logarithmic and clearly shows the appearance of large-scale (small-wavenumber) fluctuations as also seen in Figure 5 in two dimensions.

In the hydrodynamic simulations, we used bare transport coefficient values based on Enskog kinetic theory for the hard-sphere fluid [69]. For the single-component fluid with molecular mass $m = 1$, this theory gives $\eta_0 \approx 2.32$ and $\chi_0 \approx 0.053$, which corresponds to a bare Schmidt number $S_c = \nu_0/\chi_0 \approx 51$. We used the same model dependence of bare transport coefficients on concentration as for hard disks; see Equations (C-1) and (C-2). The time step was set at $\Delta t = 1$ (corresponding to viscous CFL number $\beta = \nu_0 \Delta t/\Delta x^2 \approx 0.1$). In three dimensions, the cell Peclet number is reduced with decreasing Δx, and we did not find it necessary to use any filtering.

Instead of the fully periodic domain used in the two-dimensional hard-disk simulations, here we employ the fixed-concentration boundary conditions (15) and set $c(y = 0; t) = 0$ at the bottom and $c(y = L_y; t) = 1$ at the top boundary. This emulates the sort of "open" or "reservoir" boundaries [17] that mimic conditions in experimental studies of diffusive mixing [12]. The initial condition is a fully phase-separated mixture with $c = 1$ for $y \geq L/2$ and $c = 0$ otherwise. As the mixing process continues, the diffusive interface roughens and giant concentrations appear as illustrated in Figure 7 and also observed experimentally in water-glycerol mixtures in [12]. In three dimensions, however, the diffusive interface roughness is much smaller than in two dimensions, being on the order of only 20 molecular diameters for the snapshot shown in the figure. This illustrates the importance of dimensionality when including thermal fluctuations. In particular, unlike in deterministic fluid dynamics, in fluctuating hydrodynamics, one cannot simply eliminate dimensions from consideration even in simple geometries.

Approximate theory based on the Boussinesq approximation and linearization of the equations of fluctuating hydrodynamics has been developed in [77] and applied in the analysis of experimental results on mixing in a water-glycerol mixture in the presence of gravity [12]. The simulations reported here do not make the sort of approximations necessary in analytical theories and can in principle be used to study the mixing process quantitatively. However, it is important to emphasize that in realistic liquids, such as a water-glycerol mixture, the Schmidt number is on the order of 1000. This makes explicit time-stepping schemes that fully resolve the dynamics of the velocity fluctuations infeasible. In future work, we will consider semi-implicit type-stepping methods that relax the severe time-stepping restrictions present in the explicit schemes considered here.

VII. Conclusions

The behavior of fluids is strongly affected by thermal fluctuations at scales from the microscopic to the macroscopic. Fluctuating hydrodynamics is a powerful coarse-grained model for fluid dynamics at mesoscopic and macroscopic scales at

both a theoretical and a computational level. Theoretical calculations are rather complicated in the presence of realistic spatial inhomogeneities and nontrivial boundary conditions. In numerical simulations, those effects can readily be handled; however, the large separation of time scales between different physical processes poses a fundamental difficulty. Compressible fluctuating hydrodynamics bridges the gap between molecular and hydrodynamic scales. At spatial scales not much larger than molecular, sound and momentum and heat diffusion occur at comparable time scales in both gases and liquids. At mesoscopic and larger length scales, fast pressure fluctuations due to thermally actuated sound waves are much faster than diffusive processes. It is therefore necessary to eliminate sound modes from the compressible equations. In the deterministic context, this is accomplished using low Mach number asymptotic expansion.

For homogeneous simple fluids or mixtures of dynamically identical fluids, the zeroth-order low Mach equations are the well-known incompressible Navier–Stokes equations, in which pressure is a Lagrange multiplier enforcing a divergence-free velocity field. In mixtures of dissimilar fluids, local changes in composition and temperature cause local expansion and contraction of the fluid and thus a nonzero velocity divergence. In this paper, we proposed low Mach number fluctuating equations for isothermal binary mixtures of incompressible fluids with different density or a mixture of low-density gases with different molecular masses. These equations are a straightforward generalization of the widely used incompressible fluctuating Navier–Stokes equations. In the low Mach number equations, the incompressibility constraint $\nabla \cdot \boldsymbol{v} = 0$ is replaced by $\nabla \cdot \boldsymbol{v} = -\beta(Dc/Dt)$, which ensures that compositional changes are accompanied by density changes in agreement with the fluid equation of state (EOS) at constant pressure and temperature. This seemingly simple generalization poses many nontrivial analytical and numerical challenges, some of which we addressed in this paper.

At the analytical level, the low Mach number fluctuating equations are different from the incompressible equations because the velocity divergence is directly coupled to the time derivative of the concentration fluctuations. This means that at thermodynamic equilibrium the velocity is not only white in space, a well-known difficulty with the standard equations of fluctuating hydrodynamics, but is also white in time, adding a novel type of difficulty that has not heretofore been recognized. The unphysically fast fluctuations in velocity are caused by the unphysical assumption of infinite separation of time scales between the sound and the diffusive modes. This unphysical assumption also underlies the incompressible fluctuating Navier–Stokes equations; however, in the incompressible limit $\beta \to 0$, the problem is not apparent because the component of velocity that is white in time disappears. Here we analyzed the low Mach equations at the linearized level and showed that they reproduce the slow diffusive fluctuations in the full compressible equations while eliminating the

fast pressure fluctuations. At the formal level, we suggest that a generalized Hodge decomposition can be used to separate the vortical (solenoidal) modes of velocity as the independently fluctuating variable, coupled with a gauge formulation used to treat the divergence constraint. Such nonlinear analysis is deferred for future research, and here we relied on the fact that the temporal discretization regularizes the short-time dynamics at time scales faster than the time-step size Δt.

At the numerical level, the low Mach number equations pose several distinct challenges. The first challenge is to construct conservative spatial discretizations in which density is advected in a locally conservative manner while still maintaining the equation-of-state constraint relating the local densities and composition. We accomplish this here by using a specially chosen model EOS that is linear yet still rather versatile in practice, and by advecting densities using a velocity that obeys a discrete divergence constraint. We note that, for this simplified case, the system can be modeled using only the concentration to describe the thermodynamic state. However, for more general low Mach number models, maintaining a full thermodynamic representation of the state independent of the constraint leads to more robust numerics. As in incompressible hydrodynamics, enforcing this constraint requires a Poisson pressure solver that dominates the computational cost of the algorithm. A second challenge is to construct temporal integrators that are at least second-order in time. We accomplish this here by formally introducing an unconstrained gauge formulation of the equations while at the same time taking advantage of the gauge degree of freedom to avoid ever explicitly dealing with the gauge variable. The present temporal discretizations are purely explicit and are similar in spirit to an explicit projection method. A third and remaining challenge is to design efficient temporal integrators that handle momentum diffusion, the second-fastest physical process, semi-implicitly. This poses well-known challenges even in the incompressible setting. These challenges were bypassed in recently developed temporal integrators for the incompressible fluctuating Navier–Stokes equations [73] by avoiding the splitting inherent in projection methods. Extending this type of Stokes-system approach to the low Mach equations will be the subject of future research.

One of the principal motivations for developing the low Mach number equations and our numerical implementation was to model recent experiments on the development of giant concentration fluctuations in the presence of sharp concentration gradients. We first studied giant fluctuations in a time-independent or static setting as observed experimentally by inducing a constant concentration gradient via a constant applied temperature gradient. Our simulations show that, under conditions employed in experimental studies of the diffusive mixing of water and glycerol, it is reasonable to employ the Boussinesq approximation. The results also indicate that the constant-transport-coefficient approximation that is commonly used in

theoretical calculations is appropriate if the diffusion coefficient follows a Stokes–Einstein relation, but should be used with caution in general.

We continued our study of giant concentration fluctuations by simulating the temporal evolution of a rough diffusive interface during the diffusive mixing of hard-disk fluids. Comparison between computationally intensive event-driven molecular-dynamics simulations and our hydrodynamic calculations demonstrated that the low Mach number equations of fluctuating hydrodynamics provide an accurate coarse-grained model of fluid mixing. Special care must be exercised, however, in choosing the bare transport coefficients, especially the concentration-diffusion coefficient, as these are renormalized by the fluctuations and can be strongly grid-dependent [23; 24; 26]. Some questions remain about how to define and measure the bare transport coefficients from microscopic simulations, but we show that simply comparing particle and hydrodynamic calculations at large scales is a robust technique.

The strong coupling between velocity fluctuations and diffusive transport means that deterministic models have limited utility at mesoscopic scales and even macroscopic scales in two dimensions. This implies that standard fluorescent techniques for measuring diffusion coefficients, such as fluorescence correlation spectroscopy (FCS) and fluorescence recovery after photobleaching (FRAP) [8], may not in fact be measuring material constants but rather geometry-dependent values [26]. Fluctuating hydrodynamic simulations of typical experimental simulations, however, are still out of reach due to the very large separation of time scales between mass and momentum diffusion. Surpassing this limitation requires the development of a semi-implicit temporal discretization that is stable for large time steps. Furthermore, it is also necessary to develop novel mathematical models and algorithms that are not only stable but also accurate in the presence of such large separation of scales. This is a nontrivial challenge if thermal fluctuations are to be included consistently and will be the subject of future research.

Appendix A: Linearized analysis

As discussed in more depth in [73], there are fundamental mathematical difficulties with the interpretation of the nonlinear equations of fluctuating hydrodynamics due to the roughness of the fluctuating fields. It should be remembered, however, that these equations are coarse-grained models with the coarse-graining length scale set by the size of the hydrodynamic cells used in discretizing the equations [34]. The spatial discretization removes the small length scales from the stochastic forcing and regularizes the equations. It is important to point out, however, that imposing such a small-scale regularization (smoothing) of the stochastic forcing also requires a suitable renormalization of the transport coefficients [4; 23; 26] as we discuss in more detail in Section VI.

As long as there are sufficiently many molecules per hydrodynamic cell, the fluctuations in the spatially discrete hydrodynamic variables will be small and the behavior of the nonlinear equations will closely follow that of the *linearized* equations of fluctuating hydrodynamics [73], which can be given a precise meaning [13]. It is therefore crucial to understand the linearized equations from a theoretical perspective and to analyze the behavior of the numerical schemes in the linearized setting [29].

A1. ***Compressible equations.*** Some of the most important quantities predicted by the fluctuating hydrodynamics equations are the equilibrium structure factors (static covariances) of the fluctuating fields. These can be obtained by linearizing the compressible equations (1) around a uniform reference state $\rho = \rho_0 + \delta\rho,\ c = c_0 + \delta c,$ $\boldsymbol{v} = \delta\boldsymbol{v},\ P = P_0 + \delta P$, where

$$\delta P = c_T^2[(\delta\rho) - \beta\rho(\delta c)],$$

and then applying a spatial Fourier transform [61; 29]. Owing to fluctuation-dissipation balance, the static structure factors are independent of the wavevector $\boldsymbol{k}$ at thermodynamic equilibrium,

$$\begin{aligned} S_{\rho,\rho}(\boldsymbol{k}) &= \left\langle (\widehat{\delta\rho})(\widehat{\delta\rho})^\star \right\rangle = \frac{\rho_0 k_B T_0}{c_T^2} + \beta^2 \frac{\rho_0 k_B T_0}{\mu_c}, \\ \boldsymbol{S}_{\boldsymbol{v},\boldsymbol{v}}(\boldsymbol{k}) &= \left\langle (\widehat{\delta\boldsymbol{v}})(\widehat{\delta\boldsymbol{v}})^\star \right\rangle = \rho_0^{-1} k_B T_0 \boldsymbol{I}, \\ S_{c,c}(\boldsymbol{k}) &= \left\langle (\widehat{\delta c})(\widehat{\delta c})^\star \right\rangle = \frac{k_B T_0}{\rho_0 \mu_c}. \end{aligned} \tag{A-1}$$

Note that density fluctuations do not vanish even in the incompressible limit $c_T \to \infty$ unless $\beta = 0$. While fluctuations in ρ_1 and ρ_2 are uncorrelated, the fluctuations in concentration and density are *correlated* even at equilibrium,

$$S_{c,\rho} = \left\langle (\widehat{\delta\rho})(\widehat{\delta c})^\star \right\rangle = \beta \frac{k_B T_0}{\mu_c} = \rho_0 \beta S_{c,c}.$$

We will see below that the low Mach equations correctly reproduce the static covariances of density and concentration in the limit $c_T \to \infty$.

The dynamics of the equilibrium fluctuations can also be studied by applying a Fourier–Laplace transform in time in order to obtain the dynamic structure factors (equilibrium correlation functions) as a function of wavenumber $\boldsymbol{k}$ and wave frequency ω [61; 29]. It is well-known that the dynamic spectrum of density fluctuations $S_{\rho,\rho}(\boldsymbol{k}, \omega)$ exhibits three peaks for a given $\boldsymbol{k}$: one central Rayleigh peak at small frequencies (slow concentration fluctuations) and two symmetric Brillouin peaks centered around $\omega \approx \pm c_T k$. As the fluid becomes less compressible (i.e., the speed of sound increases), there is an increasing separation of time scales between

the side and central spectral peaks. As we will see below, the low Mach equations reproduce the central peaks in the dynamic structure factors only, eliminating the side peaks and the associated stiff dynamics.

A2. ***Low Mach equations.*** We now examine the spatiotemporal correlations of the steady-state fluctuations in the low Mach number equations (8), (9), (11), and (12). In order to model the nonequilibrium setting in which giant concentration fluctuations are observed, we include a constant background concentration gradient in the equations. Note that a density gradient will accompany a concentration gradient, and this can introduce some additional terms in $\boldsymbol{F}$ depending on how $\rho\chi$ depends on concentration. For simplicity, we assume $\rho\chi$ is a constant so that the diffusive term $\nabla\cdot\boldsymbol{F}$ in (9) is simply $\rho\chi\nabla^2 c$. We also assume the viscosity η is spatially constant to get the simplified coupled velocity-concentration equations

$$\begin{aligned} D_t\boldsymbol{v} &= -\rho^{-1}\nabla\pi + \nu\nabla^2\boldsymbol{v} + \rho^{-1}(\nabla\cdot\boldsymbol{\Sigma}) + \boldsymbol{g},\\ D_t c &= \chi\nabla^2 c + \rho^{-1}(\nabla\cdot\boldsymbol{\Psi}),\\ \nabla\cdot\boldsymbol{v} &= -\beta D_t c, \end{aligned} \tag{A-2}$$

where $\nu=\eta/\rho$ and $\rho=\rho(c)$ is given by (13).

We linearize the equations (A-2) around a steady state, $c=\bar{c}+\delta c$, $\boldsymbol{v}=\bar{\boldsymbol{v}}+\delta\boldsymbol{v}=\delta\boldsymbol{v}$, and $\pi=\bar{\pi}+\delta\pi$, where the reference state is in mechanical equilibrium, $\bar{\rho}^{-1}\nabla\bar{\pi}=\boldsymbol{g}$. We denote the background concentration gradient with $\boldsymbol{h}=\nabla\bar{c}$. We additionally assume that the reference state varies very weakly on length scales of order of the wavelength and, in particular, that $\bar{\rho}$ and $\bar{c}$ are essentially constant. This allows us to drop the bars from the notation and employ a *quasiperiodic* or weak-gradient approximation [77; 24]. In the linear approximation, the EOS constraint relates density and concentration fluctuations, $\delta\rho=\rho\beta(\delta c)$. The term $\boldsymbol{v}\cdot\nabla\boldsymbol{v}$ is second-order in the fluctuations and drops out, but the advective term $\boldsymbol{v}\cdot\nabla c$ leads to a term $(\delta\boldsymbol{v})\cdot\boldsymbol{h}$ in the concentration equation. The forcing term due to gravity becomes $\rho^{-1}(\delta\rho)\boldsymbol{g}=\beta(\delta c)\boldsymbol{g}$. After a spatial Fourier transform, the linearized form of (A-2) becomes a collection of stochastic differential equations, one system of linear additive-noise equations per wavenumber,

$$\partial_t(\widehat{\delta\boldsymbol{v}}) = -i\rho^{-1}\boldsymbol{k}(\widehat{\delta\pi}) - \nu k^2(\widehat{\delta\boldsymbol{v}}) + i\rho^{-1}\boldsymbol{k}\cdot\widehat{\boldsymbol{\Sigma}} + \beta\boldsymbol{g}(\widehat{\delta c}), \tag{A-3}$$

$$\partial_t(\widehat{\delta c}) = -\boldsymbol{h}\cdot(\widehat{\delta\boldsymbol{v}}) - \chi k^2(\widehat{\delta c}) + i\rho^{-1}(\boldsymbol{k}\cdot\widehat{\boldsymbol{\Psi}}), \tag{A-4}$$

$$\hat{\boldsymbol{k}}\cdot(\widehat{\delta\boldsymbol{v}}) = -\beta\big[i\chi k(\widehat{\delta c}) + \rho^{-1}(\hat{\boldsymbol{k}}\cdot\widehat{\boldsymbol{\Psi}})\big]. \tag{A-5}$$

Replacing the right side of (A-5) with zero leads to the incompressible approximation used in [77], corresponding to the Boussinesq approximation of taking the limit $\beta\to 0$ while keeping the product βg constant.

Equilibrium fluctuations. Let us first compare the dynamics of the equilibrium fluctuations ($\boldsymbol{h} = \mathbf{0}$) in the low Mach equations with those in the complete compressible equations. For simplicity of notation, we will continue to use the hat symbol to denote the space-time Fourier transform.

In the wavenumber-frequency $(\boldsymbol{k}, \omega)$ Fourier domain, the concentration fluctuations in the absence of a gradient are obtained from (A-4),

$$\widehat{\delta c}(\boldsymbol{k}, \omega) = \frac{i\rho^{-1}k}{i\omega + \chi k^2}(\hat{\boldsymbol{k}} \cdot \widehat{\boldsymbol{\Psi}}),$$

which is the same as the compressible equations. The density fluctuations follow the concentration fluctuations, $\widehat{\delta\rho} = \rho\beta\widehat{\delta c}$, and the dynamic structure factor for density shows the same central Rayleigh peak as obtained from the isothermal compressible equations [61],

$$S_{\rho,\rho}(\boldsymbol{k}, \omega) = \frac{\beta^2 k^2}{\omega^2 + \chi^2 k^4}\langle \widehat{\boldsymbol{\Psi}}\widehat{\boldsymbol{\Psi}}^\star \rangle = \beta^2(\rho\mu_c^{-1}k_B T)\frac{2\chi k^2}{\omega^2 + \chi^2 k^4},$$

where we used (3) for the covariance of $\widehat{\boldsymbol{\Psi}}$. This shows that the low Mach number equations correctly reproduce the slow fluctuations (small ω) in density and concentration while eliminating the side Brillouin peaks associated with the fast isentropic pressure fluctuations.

The fluctuations in velocity, however, are different between the compressible and low Mach number equations. Let us first examine the transverse (solenoidal) component of velocity $\widehat{\delta\boldsymbol{v}}_s = \widehat{\boldsymbol{\mathcal{P}}}\widehat{\delta\boldsymbol{v}}$, where $\boldsymbol{\mathcal{P}}$ is the constant-density orthogonal projection onto the space of divergence-free velocity fields ($\widehat{\boldsymbol{\mathcal{P}}} = \boldsymbol{I} - k^{-2}(\boldsymbol{k}\boldsymbol{k}^\star)$ in Fourier space). Applying the projection operator to the velocity equation (A-3) shows that the fluctuations of the solenoidal modes are the same as in the incompressible approximation,

$$\partial_t(\widehat{\delta\boldsymbol{v}}_s) = -\nu k^2(\widehat{\delta\boldsymbol{v}}_s) + i\rho^{-1}\boldsymbol{k} \cdot \widehat{\boldsymbol{\mathcal{P}}}\widehat{\boldsymbol{\Sigma}} + \beta\widehat{\boldsymbol{\mathcal{P}}}\boldsymbol{g}(\widehat{\delta c}).$$

The fluctuations of the compressive velocity component $\widehat{\delta v_l} = \hat{\boldsymbol{k}} \cdot (\widehat{\delta\boldsymbol{v}})$, on the other hand, are driven by the stochastic mass flux $\widehat{\boldsymbol{\Psi}}$ as seen from (A-5) at thermodynamic equilibrium,

$$\widehat{\delta v_l} = \frac{i\omega\beta\rho^{-1}}{i\omega + \chi k^2}(\hat{\boldsymbol{k}} \cdot \widehat{\boldsymbol{\Psi}}).$$

The dynamic structure factor (space-time Fourier spectrum) of the longitudinal component

$$S_{v,v}^{(l)} = \left\langle (\widehat{\delta v_l})(\widehat{\delta v_l})^\star \right\rangle \sim \frac{\beta^2\omega^2}{(\omega^2 + \chi^2 k^4)}$$

does not decay to zero as $\omega \to \infty$. This indicates that the fluctuations of velocity are not only white in space but also white in time. In the incompressible approximation, $\beta \to 0$ so that the longitudinal velocity fluctuations vanish and the static spectrum of the velocity fluctuations is equal to the projection operator, $\boldsymbol{S}_{\boldsymbol{v},\boldsymbol{v}} = \widehat{\boldsymbol{\mathcal{P}}}$ [73]. In the compressible equations, the dynamic structure factor for the longitudinal component of velocity decays to zero as $\omega \to \infty$ because it has two sound (Brillouin) peaks centered around $\omega \approx c_T k$ in addition to the central diffusive (Rayleigh) peak. The low Mach number equations reproduce the central peak (slow fluctuations) correctly, replacing the side peaks with a flat spectrum for large ω. The origin of this unphysical behavior is the unjustified assumption of infinite separation of time scales between the propagation of sound and the diffusion of mass, momentum, and energy. In reality, the same molecular motion underlies all of these processes and the incompressible or the low Mach number equations cannot be expected to reproduce the correct physical behavior at very short time scales ($\omega \gtrsim c_T k$).

Nonequilibrium fluctuations. If we neglect the term involving $\widehat{\boldsymbol{\Psi}}$ in (A-5) and eliminate the Lagrange multiplier (nonthermodynamic pressure) π using (A-5), we obtain the linearized velocity equation in Fourier space

$$\begin{aligned}\partial_t(\widehat{\delta \boldsymbol{v}}) = &-\nu k^2(\widehat{\delta \boldsymbol{v}}) + i\rho^{-1}\boldsymbol{k}\cdot\widehat{\boldsymbol{\mathcal{P}}}\widehat{\boldsymbol{\Sigma}} + \beta(\widehat{\delta c})\widehat{\boldsymbol{\mathcal{P}}}\boldsymbol{g} \\ &- i\beta\chi[\boldsymbol{h}\cdot(\widehat{\delta \boldsymbol{v}})]\boldsymbol{k} + i\beta\chi(\nu-\chi)k^2(\widehat{\delta c})\boldsymbol{k}. \end{aligned} \tag{A-6}$$

It is straightforward to obtain the steady-state covariances (static structure factors) in the presence of a concentration gradient from the linearized system of velocity-concentration equations (A-4) and (A-6) [29]. The procedure amounts to solving a linear system for three covariances (velocity-velocity, concentration-concentration, and velocity-concentration). These types of calculations are particularly well-suited for modern computer algebra systems like Maple and can be carried out for arbitrary wavenumber and background concentration gradient. We omit the full solution for brevity.

Experiments measure the steady-state spectrum of concentration fluctuations averaged along the gradient [12; 75], and we will therefore focus on wavenumbers perpendicular to the gradient, $\boldsymbol{k}\cdot\boldsymbol{h} = 0$. A straightforward calculation shows that the concentration fluctuations are enhanced as the square of the applied gradient,

$$\begin{aligned} S_{c,c}(\boldsymbol{k}) &= \left\langle(\widehat{\delta c})(\widehat{\delta c})^\star\right\rangle \\ &= \frac{k_B T_0}{\rho_0 \mu_c} + \frac{\nu k_B T}{\rho(\nu+\chi)\left[(\nu\chi k_\perp^4 + h_\parallel g\beta) + \beta^2(\chi^3\nu/(\nu+\chi)^2)k_\perp^2 h_\perp^2\right]}\, h_\parallel^2, \end{aligned} \tag{A-7}$$

where $\perp$ and $\parallel$ denote the perpendicular and parallel components relative to gravity, respectively. The term in the denominator involving $h_\perp$ comes from the low Mach number constraint (11) and is usually negligible since the concentration gradient is

parallel to gravity or $\chi/\nu \ll 1$. Without this term, the result (A-7) is the same result as obtained in [77] and shows that fluctuations at wavenumbers below $k_\perp^4 = h_\parallel g\beta/(\nu\chi)$ are suppressed by gravity as we study numerically in Section V.

Appendix B: Spatial filtering

In our spatial discretization, we use centered differencing for the advective terms because this leads to a skew-adjoint discretization of advection [54] that maintains discrete fluctuation-dissipation balance in the spatially discretized stochastic equations [29; 18]. It is well-known that centered discretizations of advection do not preserve monotonicity properties of the underlying PDEs in the deterministic setting unlike one-sided (upwind) discretizations. Therefore, our spatiotemporal discretization can lead to unphysical oscillations of the concentration and density in cases where the cell Peclet number $\mathrm{Pe} = \Delta x\|\boldsymbol{v}\|/\chi$ is large.

In the deterministic setting, Pe can always be decreased by reducing Δx and resolving the fine-scale dissipative features of the flow. However, in the stochastic setting, the magnitude of the fluctuating velocities at equilibrium is

$$\langle(\delta v)^2\rangle \sim \frac{k_B T}{\rho \Delta V},$$

where ΔV is the volume of the hydrodynamic cell. Therefore, in two dimensions, the characteristic advection velocity magnitude is $\|\boldsymbol{v}\| \sim \Delta x^{-1}$. This means that in two dimensions Pe is independent of the grid size and reducing Δx cannot fix problems that may arise due to a large cell Peclet number. For some of the simulations reported in Section VI, we have found it necessary to implement a spatial filtering procedure to reduce the magnitude of the fluctuating velocities while preserving their spectrum as well as possible at small wavenumbers.

The filtering procedure consists of applying a local averaging operation to the spatially discretized random fields $\boldsymbol{\mathcal{W}}$ and $\widetilde{\boldsymbol{\mathcal{W}}}$ independently along each Cartesian direction. This local averaging smooths the random forcing and thus reduces the spectrum of the random forcing at larger wavenumbers. The specific filters we use are taken from [46]. For stencil width $w_F = 2$, filtering a discrete field W in one dimension takes the form

$$W_i \leftarrow \tfrac{5}{8}W_i + \tfrac{1}{4}(W_{i-1} + W_{i+1}) - \tfrac{1}{16}(W_{i-2} + W_{i+2}).$$

In Fourier space, for discrete wavenumber $\Delta k = k\Delta x$, this local averaging multiplies the spectrum of W by $\mathcal{F}(\Delta k) = 1 + O(\Delta k^4)$ and therefore maintains the second-order accuracy of the spatial discretization. At the same time, the filtering reduces the variance of the fluctuating fields by about a factor of two in one dimension (a larger factor in two dimensions). The spectrum of the fluctuations can be preserved

even more accurately if a stencil of width $w_F = 4$ is used for the local averaging,

$$W_i \leftarrow \tfrac{93}{128} W_i + \tfrac{7}{32}(W_{i-1} + W_{i+1}) - \tfrac{7}{64}(W_{i-2} + W_{i+2}) + \tfrac{1}{32}(W_{i-3} + W_{i+3}) - \tfrac{1}{256}(W_{i-4} + W_{i+4}),$$

giving a sixth-order-accurate filter $\mathcal{F}(\Delta k) = 1 + O(\Delta k^8)$ and a reduction of the variance by about a third in one dimension. In two and three dimensions, the filtering operators are simple tensor products of one-dimensional filtering operators. Note that we only use these filters with periodic boundary conditions. One can, of course, also use Fourier-transform techniques to filter out high-frequency components from the stochastic mass and momentum fluxes.

Appendix C: Extracting transport properties from molecular dynamics

The hydrodynamic simulations described in Section VI require as input transport coefficients, notably, the shear viscosity η and diffusion coefficient χ, which need to be extracted from the underlying microscopic (molecular) dynamics. This is a very delicate and important step that has not, to our knowledge, been carefully performed in previous studies. In this appendix, we give details about the procedure we developed for this purpose.

C1. ***Viscosity ν.*** As discussed in more detail in [24; 26], the transport coefficients in fluctuating hydrodynamics are not universal material constants but rather depend on the spatial scale (degree of coarse-graining) under question. We emphasize that this scale-dependent renormalization is not a molecular scale effect but rather an effect arising out of hydrodynamic fluctuations and persists even at the hydrodynamic scales we are examining here. The best way to define and measure transport coefficients is by examining the dynamics of *equilibrium* fluctuations, specifically, by examining the *dynamic structure factors* of the hydrodynamic fields [61], i.e., the equilibrium averages of the spatiotemporal Fourier spectra of the fluctuating hydrodynamic fields. For a hydrodynamic variable ξ that is transported by a purely diffusive process, the spectrum of the fluctuations at a given wavenumber k and wave frequency ω is expected to be a Lorentzian peak of the form

$$S_x(k, \omega) = \langle \hat{x}(k, \omega)\, \hat{x}^\star(k, \omega) \rangle \sim [\omega^2 + \zeta^2 k^4]^{-1},$$

where in general the diffusion constant $\zeta(k)$ depends on the wavenumber k (wavelength $\lambda = 2\pi/k$). We can therefore estimate the diffusion coefficient χ by fitting a Lorentzian peak to $S_c(k, \omega)$ for different k's (i.e., $\xi \equiv c$). Similarly, we can estimate the kinematic viscosity $\nu = \eta/\rho$ by fitting a Lorentzian curve to dynamic structure factors for the scaled vorticity, $\xi \equiv k^{-1}(\nabla \times \boldsymbol{v})_z$.

We performed long equilibrium molecular-dynamics simulations of systems corresponding to a grid of $N_c = 32$ hydrodynamic cells and then calculated the

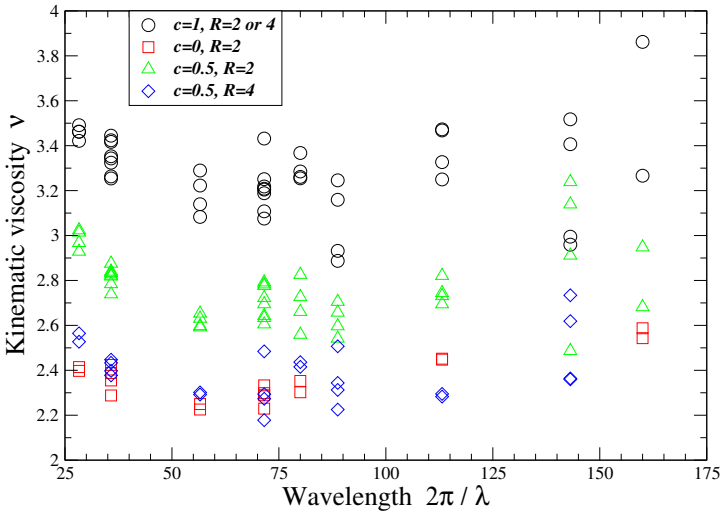

Figure 8. Estimates of the momentum diffusion coefficient (viscosity) $\nu = \eta/\rho$ obtained from the width of the central peak in the dynamic structure factor of vorticity. A collection of 24 distinct discrete wavenumbers $\boldsymbol{k}$ were used and the width of the peaks estimated using a nonlinear least-squares Lorentzian fit.

discrete spatiotemporal Fourier spectrum of the hydrodynamic fields at a collection of discrete wavenumbers $\boldsymbol{k}$. Since these simulations are at equilibrium, the systems are well-mixed; specifically, the initial configurations were generated by randomly assigning a species label to each particle. We then performed a nonlinear least-squares Lorentzian fit in ω for each $\boldsymbol{k}$ and estimated the width of the Lorentzian peak. The results for the dynamics of the equilibrium vorticity fluctuations are shown in Figure 8. We see that kinematic viscosity is relatively constant for a broad range of wavelengths, consistent with fluctuating hydrodynamics calculations [51] and previous molecular-dynamics simulations [38]. For the pure component-one fluid, $c = 1$, with density $\rho \approx 0.764$, the figure shows $\nu \approx 3.3$. We therefore used $\eta_1 \approx 0.764 \cdot 3.3 \approx 2.5$ in all of the hydrodynamic runs reported in Section VI. This is about 20% higher than the prediction of the simple Enskog kinetic theory [42], $\eta \approx 2.06$, and is consistent with the estimates reported in [38]. Because the diffusion coefficient is small at the densities we study, more specifically because the Schmidt number $S_c = \nu/\chi$ is larger than 10, we were unable to obtain reliable estimates for $\chi(k)$ from the dynamic structure factor for concentration.

Simple dimensional analysis or kinetic theory shows that $\eta \sim \sqrt{m}$. Since the disks of the two species have equal diameters, the viscosity of the pure second fluid component is

$$\eta_2 = \eta_1 \sqrt{\frac{m_2}{m_1}} = \eta_1 \sqrt{R}. \tag{C-1}$$

There is no simple theory that accurately predicts the concentration dependence of the viscosity of a hard-disk mixture at higher densities [69]. To our knowledge, there is no published Enskog kinetic-theory calculations for hard-disk mixtures in two dimensions even for the simpler case of equal diameters. As an approximation to the true dependence, we employed a simple linear interpolation of the *kinematic* viscosity $\nu(c) = \eta(c)/\rho$ as a function of the mass concentration c between the two known values $\nu_1 = \nu(c = 1) \approx 3.3$ and $\nu_2 = \nu(c = 0) = \nu_1/\sqrt{R}$. The numerical results for mixtures with mass ratios $R = 2$ and $R = 4$ in Figure 8 are consistent with this approximation to within the large error bars. For example, for $c = 1/2$ and $R = 4$, the interpolation gives $\nu = 3 \cdot 3.3/4 \approx 2.5$, which is in reasonable agreement with the numerical estimate.

C2. ***Diffusion coefficient*** χ**.** For the interspecies diffusion coefficient χ, which we emphasize is distinct from the self-diffusion coefficients for particles of either species, Enskog kinetic theory predicts no concentration dependence and a simple scaling with the mass ratio [69],

$$\chi(R) = \chi(R = 1)\sqrt{\frac{1+R}{2R}}. \tag{C-2}$$

This particular dependence on mass ratio R comes from the fact that the average relative speed between particles of different species is $\sim \sqrt{k_B T/m_R}$, where $m_R = 2m_1m_2/(m_1 + m_2)$ is the reduced molecular mass. We have assumed in our hydrodynamic calculations that the diffusion coefficient is independent of concentration and follows (C-2). The only input to the hydrodynamic calculation is the bare self-diffusion coefficient for the pure-component fluid, $\chi_0(R=1)$. Diffusion is strongly renormalized by thermal fluctuations, and fluctuating hydrodynamics theory and simulations predict a strong dependence of the diffusion coefficient χ on the wavelength [24], consistent with molecular-dynamics results [38].

In order to estimate the appropriate value of the bare diffusion coefficient χ_0, we numerically solved an inverse problem. Using simple bisection, we looked for the value of χ_0 that leads to best agreement for the average or "macroscopic" diffusion (mixing) between the particle and continuum simulations. Specifically, we calculated the density of the first species $\rho_1^{(h)}(y)$ along the y-direction by averaging ρ_1 in each horizontal row of hydrodynamic cells; see (50). The results for $\rho_1^{(h)}$ for mass ratios $R = 1$ and $R = 4$ are shown in Figure 9 at different points in time for systems of size $N_c = 64$ cells. The figures show the expected sort of diffusive-mixing profile, which is exactly what would be used in experiments to measure diffusion coefficients using fluorescent techniques such as fluorescence recovery after photobleaching (FRAP) [8]. This macroscopic measurement smooths over the fluctuations (roughness) of the diffusive interface and only measures an effective diffusion coefficient at the scale of the domain length L. If deterministic

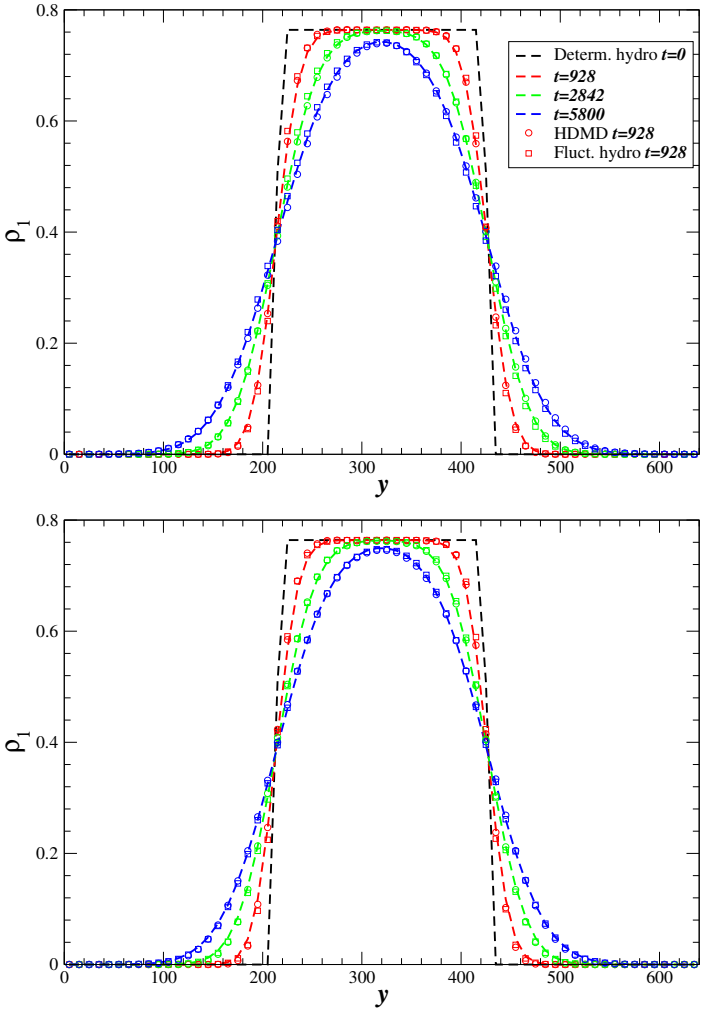

Figure 9. Top: diffusive evolution of the horizontally averaged density $\rho_1^{(h)}(y)$ for a system of size $N_c = 64$ hydrodynamic cells and density ratio $R = 1$ as obtained from HDMD simulations (circles, averaged over 64 runs), deterministic hydrodynamics with $\chi_{\text{eff}} = 0.2$ (dashed lines), and fluctuating hydrodynamics with $\chi_0 = 0.09$ (squares, averaged over 64 runs). Error bars are comparable to the symbol size and not shown for clarity. Bottom: same as the top panel except the density ratio is $R = 2$ and the transport coefficients are adjusted according to (C-1)–(C-2).

hydrodynamics is employed, $\rho_1^{(h)}(y)$ is the solution of a one-dimensional system of equations obtained by simply deleting the stochastic forcing and the x-dependence in the low Mach equations. Instead of solving this system analytically, we employed our spatiotemporal discretization with fluctuations turned off and with an effective diffusion coefficient $\chi = \chi_{\text{eff}}$ that accounts for the renormalization of the diffusion coefficient by the thermal fluctuations.

By matching the profile $\rho_1^{(h)}(y)$ between the HDMD and the fluctuating and deterministic hydrodynamic simulations at mass ratio $R = 1$ and system size $N_c = 64$ cells, we obtained estimates for the bare χ_0 and the renormalized χ_{eff} coefficients (see Figure 9 on the previous page). The best estimate for the bare diffusion coefficient based on this matching in the absence of filtering is $\chi_0 = 0.09 \pm 0.01$. This compares reasonably well to the prediction of Enskog theory [42] of $\chi \approx 0.08$ as well as to the measurement of the self-diffusion coefficient for a periodic system with 169 disks reported in [38], $\chi \approx 0.14$ (recall that a single hydrodynamic cell in our case contains about 76 particles). When a five-point filter is employed, the estimate is $\chi_0(w_F = 2) \approx 0.12$, and when a nine-point filter is employed, $\chi_0(w_F = 4) \approx 0.11$. The estimated renormalized diffusion coefficient is much larger, $\chi_{\text{eff}} \approx 0.20 \pm 0.01$, consistent with a rough estimate based on the simple theory presented in [24],

$$\chi_{\text{eff}} \approx \chi_0 + \frac{k_B T}{4\pi\rho(\nu + \chi_0)} \ln\Big(\frac{N_c}{3}\Big) \approx \begin{cases} 0.18 & \text{for } N_c = 64, \\ 0.20 & \text{for } N_c = 128. \end{cases}$$

To within statistical accuracy, we were not able to detect the increase in the estimated diffusion coefficients when using the larger systems of size $N_c = 128$ cells; however, for $N_c = 32$, it was clear that χ_{eff} is reduced.

It is important to emphasize that χ_{eff} is not a material constant but rather depends on the details of the problem in question, in particular, the system geometry and size and boundary conditions [26]. By contrast, χ_0 is a constant for a given spatial discretization, and one can use the same number for different scenarios so long as the hydrodynamic cell size and the filter are kept fixed. Unlike deterministic hydrodynamics, which presents an incomplete picture of diffusion, fluctuating hydrodynamics correctly accounts for the important contribution of the thermal velocity fluctuations and the roughness of the diffusive interface seen in Figure 3.

Acknowledgments

We would like to thank Boyce Griffith and Mingchao Cai for helpful comments. J. Bell, A. Nonaka, and A. Garcia were supported by the DOE Applied Mathematics Program of the DOE Office of Advanced Scientific Computing Research under the U.S. Department of Energy under contract number DE-AC02-05CH11231. A. Donev was supported in part by the National Science Foundation under grant DMS-1115341 and the Office of Science of the U.S. Department of Energy through an Early Career Award (number DE-SC0008271). T. Fai wishes to acknowledge the support of the DOE Computational Science Graduate Fellowship under grant number DE-FG02-97ER25308. Y. Sun was supported by the National Science Foundation under award OCI 1047734.

References

[1] A. S. Almgren, A. J. Aspden, J. B. Bell, and M. L. Minion, *On the use of higher-order projection methods for incompressible turbulent flow*, SIAM J. Sci. Comput. **35** (2013), no. 1, B25–B42. MR 3033070 Zbl 1264.76032

[2] A. S. Almgren, J. B. Bell, P. Colella, L. H. Howell, and M. L. Welcome, *A conservative adaptive projection method for the variable density incompressible Navier–Stokes equations*, J. Comput. Phys. **142** (1998), no. 1, 1–46. MR 99k:76096 Zbl 0933.76055

[3] P. J. Atzberger, *Stochastic Eulerian Lagrangian methods for fluid-structure interactions with thermal fluctuations*, J. Comput. Phys. **230** (2011), no. 8, 2821–2837. MR 2012c:74040 Zbl 05909504

[4] D. Bedeaux and P. Mazur, *Renormalization of the diffusion coefficient in a fluctuating fluid, I*, Physica **73** (1974), no. 3, 431–458. MR 53 #10059

[5] J. B. Bell, P. Colella, and H. M. Glaz, *A second-order projection method for the incompressible Navier–Stokes equations*, J. Comput. Phys. **85** (1989), no. 2, 257–283. MR 90i:76002 Zbl 0681.76030

[6] J. B. Bell, A. L. Garcia, and S. A. Williams, *Computational fluctuating fluid dynamics*, ESAIM Math. Model. Numer. Anal. **44** (2010), no. 5, 1085–1105. MR 2011h:76030 Zbl 05798944

[7] L. Bocquet and E. Charlaix, *Nanofluidics, from bulk to interfaces*, Chem. Soc. Rev. **39** (2010), no. 3, 1073–1095.

[8] K. Braeckmans, L. Peeters, N. N. Sanders, S. C. De Smedt, and J. Demeester, *Three-dimensional fluorescence recovery after photobleaching with the confocal scanning laser microscope*, Biophys. J. **85** (2003), no. 4, 2240–2252.

[9] D. Brogioli, *Giant fluctuations in diffusion in freely-suspended liquid films*, preprint, 2011. arXiv 1103.4763v2

[10] M. Cai, A. J. Nonaka, J. B. Bell, B. E. Griffith, and A. Donev, *Efficient variable-coefficient finite-volume Stokes solvers*, preprint, 2013. arXiv 1308.4605v1

[11] F. Croccolo, H. Bataller, and F. Scheffold, *A light scattering study of non equilibrium fluctuations in liquid mixtures to measure the soret and mass diffusion coefficient*, J. Chem. Phys. **137** (2012), #234202.

[12] F. Croccolo, D. Brogioli, A. Vailati, M. Giglio, and D. S. Cannell, *Nondiffusive decay of gradient-driven fluctuations in a free-diffusion process*, Phys. Rev. E **76** (2007), no. 4, 041112.

[13] G. Da Prato, *Kolmogorov equations for stochastic PDEs*, Birkhäuser, 2004. MR 2005m:60002 Zbl 1066.60061

[14] B. Davidovitch, E. Moro, and H. A. Stone, *Spreading of viscous fluid drops on a solid substrate assisted by thermal fluctuations*, Phys. Rev. Lett. **95** (2005), no. 24, 244505.

[15] M. S. Day and J. B. Bell, *Numerical simulation of laminar reacting flows with complex chemistry*, Combust. Theory Model. **4** (2000), no. 4, 535–556. Zbl 0970.76065

[16] R. Delgado-Buscalioni, E. Chacon, and P. Tarazona, *Hydrodynamics of nanoscopic capillary waves*, Phys. Rev. Lett. **101** (2008), no. 10, 106102.

[17] R. Delgado-Buscalioni, *Tools for multiscale simulation of liquids using open molecular dynamics*, Numerical analysis of multiscale computations (B. Engquist, O. Runborg, and Y.-H. R. Tsai, eds.), Lect. Notes Comput. Sci. Eng., no. 82, Springer, Heidelberg, 2012, pp. 145–166. MR 3075795 Zbl 1243.82005

[18] S. Delong, B. E. Griffith, E. Vanden-Eijnden, and A. Donev, *Temporal integrators for fluctuating hydrodynamics*, Phys. Rev. E **87** (2013), no. 3, 033302.

[19] G. D'Errico, O. Ortona, F. Capuano, and V. Vitagliano, *Diffusion coefficients for the binary system glycerol + water at 25°c: a velocity correlation study*, J. Chem. Engin. Data **49** (2004), no. 6, 1665–1670.

[20] F. Detcheverry and L. Bocquet, *Thermal fluctuations in nanofluidic transport*, Phys. Rev. Lett. **109** (2012), 024501.

[21] F. Detcheverry and L. Bocquet, *Thermal fluctuations of hydrodynamic flows in nanochannels*, Phys. Rev. E **88** (2013), no. 1, 012106.

[22] A. Donev, B. J. Alder, and A. L. Garcia, *Stochastic hard-sphere dynamics for hydrodynamics of nonideal fluids*, Phys. Rev. Lett. **101** (2008), 075902.

[23] A. Donev, J. B. Bell, A. de la Fuente, and A. L. Garcia, *Diffusive transport by thermal velocity fluctuations*, Phys. Rev. Lett. **106** (2011), no. 20, 204501.

[24] ———, *Enhancement of diffusive transport by non-equilibrium thermal fluctuations*, J. Stat. Mech. Theor. Exp. (2011), P06014.

[25] A. Donev, T. G. Fai, and E. Vanden-Eijnden, *Reversible diffusion by thermal fluctuations*, preprint, 2013. arXiv 1306.3158v3

[26] ———, *A reversible mesoscopic model of diffusion in liquids: from giant fluctuations to Fick's law*, J. Stat. Mech. Theor. Exp. (2014), P04004.

[27] A. Donev, S. Torquato, and F. H. Stillinger, *Neighbor list collision-driven molecular dynamics simulation for nonspherical hard particles, I: Algorithmic details*, J. Comput. Phys. **202** (2005), no. 2, 737–764. MR 2006e:82093 Zbl 1067.82061

[28] ———, *Neighbor list collision-driven molecular dynamics simulation for nonspherical hard particles, II: Applications to ellipses and ellipsoids*, J. Comput. Phys. **202** (2005), no. 2, 765–793. MR 2006e:82094 Zbl 1067.82062

[29] A. Donev, E. Vanden-Eijnden, A. L. Garcia, and J. B. Bell, *On the accuracy of finite-volume schemes for fluctuating hydrodynamics*, Commun. Appl. Math. Comput. Sci. **5** (2010), no. 2, 149–197. MR 2012d:65017 Zbl 1277.76089

[30] J. R. Dorfman, T. R. Kirkpatrick, and J. V. Sengers, *Generic long-range correlations in molecular fluids*, Annu. Rev. Phys. Chem. **45** (1994), 213–239.

[31] B. Dünweg and A. J. C. Ladd, *Lattice Boltzmann simulations of soft matter systems*, Advanced computer simulation approaches for soft matter sciences, III (C. Holm and K. Kremer, eds.), Advances in Polymer Science, no. 221, Springer, Berlin, 2009, pp. 89–166.

[32] D. R. Durran, *Improving the anelastic approximation*, J. Atmos. Sci. **46** (1989), no. 11, 1453–1461.

[33] W. E and J.-G. Liu, *Gauge method for viscous incompressible flows*, Commun. Math. Sci. **1** (2003), no. 2, 317–332. MR 2004c:76039 Zbl 1160.76329

[34] P. Español, J. G. Anero, and I. Zúñiga, *Microscopic derivation of discrete hydrodynamics*, J. Chem. Phys. **131** (2009), 244117.

[35] P. Español and I. Zúñiga, *On the definition of discrete hydrodynamic variables*, J. Chem. Phys. **131** (2009), 164106.

[36] A. L. Garcia, M. Malek Mansour, G. C. Lie, M. Mareschal, and E. Clementi, *Hydrodynamic fluctuations in a dilute gas under shear*, Phys. Rev. A **36** (1987), no. 9, 4348–4355.

[37] A. L. Garcia, *Estimating hydrodynamic quantities in the presence of microscopic fluctuations*, Commun. Appl. Math. Comput. Sci. **1** (2006), 53–78. MR 2007c:82078 Zbl 1111.82051

[38] R. García-Rojo, S. Luding, and J. J. Brey, *Transport coefficients for dense hard-disk systems*, Phys. Rev. E **74** (2006), no. 6, 061305.

[39] C. W. Gardiner and M. L. Steyn-Ross, *Adiabatic elimination in stochastic systems, I*, Phys. Rev. A **29** (1984), 2814–2822.

[40] ———, *Adiabatic elimination in stochastic systems, II*, Phys. Rev. A **29** (1984), 2823–2833.

[41] ———, *Adiabatic elimination in stochastic systems, III*, Phys. Rev. A **29** (1984), 2834–2844.

[42] D. M. Gass, *Enskog theory for a rigid disk fluid*, J. Chem. Phys. **54** (1971), no. 5, 1898–1902.

[43] F. H. Harlow and J. E. Welch, *Numerical calculation of time-dependent viscous incompressible flow of fluids with free surfaces*, Phys. Fluids **8** (1965), 2182–2189.

[44] Y. Hennequin, D. G. A. L. Aarts, J. H. van der Wiel, G. Wegdam, J. Eggers, H. N. W. Lekkerkerker, and D. Bonn, *Drop formation by thermal fluctuations at an ultralow surface tension*, Phys. Rev. Lett. **97** (2006), no. 24, 244502.

[45] C. Hijón, P. Español, E. Vanden-Eijnden, and R. Delgado-Buscalioni, *Mori–Zwanzig formalism as a practical computational tool*, Faraday Discuss. **144** (2010), 301–322.

[46] C. A. Kennedy and M. H. Carpenter, *Several new numerical methods for compressible shear-layer simulations*, Appl. Num. Math. **14** (1994), no. 4, 397–433. MR 95d:76073 Zbl 0804.76062

[47] S. Klainerman and A. Majda, *Compressible and incompressible fluids*, Comm. Pure Appl. Math. **35** (1982), no. 5, 629–651. MR 84a:35264 Zbl 0478.76091

[48] L. D. Landau and E. M. Lifshitz, *Fluid mechanics*, Course of Theoretical Physics, no. 6, Pergamon Press, Oxford, 1959.

[49] ———, *Statistical physics, I*, 3rd ed., Course of Theoretical Physics, no. 5, Butterworth–Heinemann, Oxford, 1980.

[50] J. Lowengrub and L. Truskinovsky, *Quasi-incompressible Cahn–Hilliard fluids and topological transitions*, Proc. R. Soc. Lond. Ser. A **454** (1998), no. 1978, 2617–2654. MR 2000e:82022 Zbl 0927.76007

[51] J. Lutsko and J. W. Dufty, *Mode-coupling contributions to the nonlinear shear viscosity*, Phys. Rev. A **32** (1985), 1229–1231.

[52] A. Majda and J. Sethian, *The derivation and numerical solution of the equations for zero Mach number combustion*, Combust. Sci. Technol. **42** (1985), no. 3–4, 185–205.

[53] M. Mareschal, M. Malek Mansour, G. Sonnino, and E. Kestemont, *Dynamic structure factor in a nonequilibrium fluid: a molecular-dynamics approach*, Phys. Rev. A **45** (1992), 7180–7183.

[54] Y. Morinishi, T. S. Lund, O. V. Vasilyev, and P. Moin, *Fully conservative higher order finite difference schemes for incompressible flow*, J. Comput. Phys. **143** (1998), no. 1, 90–124. MR 99a:76100 Zbl 0932.76054

[55] M. Moseler and U. Landman, *Formation, stability, and breakup of nanojets*, Science **289** (2000), no. 5482, 1165–1169.

[56] B. Müller, *Low-Mach-number asymptotics of the Navier–Stokes equations*, J. Eng. Math. **34** (1998), no. 1–2, 97–109. MR 99f:76111 Zbl 0924.76095

[57] A. Naji, P. J. Atzberger, and F. L. H. Brown, *Hybrid elastic and discrete-particle approach to biomembrane dynamics with application to the mobility of curved integral membrane proteins*, Phys. Rev. Lett. **102** (2009), no. 13, 138102.

[58] F. Nicoud, *Conservative high-order finite-difference schemes for low-Mach number flows*, J. Comput. Phys. **158** (2000), no. 1, 71–97. MR 2000j:76112 Zbl 0973.76068

[59] H. Noguchi, N. Kikuchi, and G. Gompper, *Particle-based mesoscale hydrodynamic techniques*, Europhys. Lett. **78** (2007), 10005.

[60] J. M. Ortiz de Zárate and J. V. Sengers, *On the physical origin of long-ranged fluctuations in fluids in thermal nonequilibrium states*, J. Stat. Phys. **115** (2004), no. 5–6, 1341–1359. Zbl 1157.76308

[61] ———, *Hydrodynamic fluctuations in fluids and fluid mixtures*, Elsevier, Amsterdam, 2006.

[62] H. C. Öttinger, *Beyond equilibrium thermodynamics*, Wiley, Hoboken, NJ, 2005.

[63] R. B. Pember, L. H. Howell, J. B. Bell, P. Colella, W. Y. Crutchfield, W. A. Fiveland, and J. P. Jessee, *An adaptive projection method for unsteady, low-Mach number combustion*, Combust. Sci. Technol. **140** (1998), no. 1–6, 123–168.

[64] C. S. Peskin, G. M. Odell, and G. F. Oster, *Cellular motions and thermal fluctuations: the Brownian ratchet*, Biophys. J. **65** (1993), no. 1, 316–324.

[65] P. Rauwoens, J. Vierendeels, E. Dick, and B. Merci, *A conservative discrete compatibility-constraint low-Mach pressure-correction algorithm for time-accurate simulations of variable density flows*, J. Comput. Phys. **228** (2009), no. 13, 4714–4744. MR 2010g:65123 Zbl 05581929

[66] R. G. Rehm and H. R. Baum, *The equations of motion for thermally driven buoyant flows*, J. Res. Natl. Bur. Stand. **83** (1978), 297–308. Zbl 0433.76072

[67] T. Schneider, N. Botta, K. J. Geratz, and R. Klein, *Extension of finite volume compressible flow solvers to multi-dimensional, variable density zero Mach number flows*, J. Comput. Phys. **155** (1999), no. 2, 248–286. MR 2000g:76081 Zbl 0968.76054

[68] B. Z. Shang, N. K. Voulgarakis, and J.-W. Chu, *Fluctuating hydrodynamics for multiscale simulation of inhomogeneous fluids: mapping all-atom molecular dynamics to capillary waves*, J. Chem. Phys. **135** (2011), 044111.

[69] C. M. Silva and H. Liu, *Modelling of transport properties of hard sphere fluids and related systems, and its applications*, Theory and simulation of hard-sphere fluids and related systems (A. Mulero, ed.), Lect. Notes Phys., no. 753, Springer, Berlin, 2008, pp. 383–492. MR 2503513

[70] M. Skoge, A. Donev, F. H. Stillinger, and S. Torquato, *Packing hyperspheres in high-dimensional Euclidean spaces*, Phys. Rev. E **74** (2006), no. 4, 041127. MR 2007j:82048

[71] P. T. Sumesh, I. Pagonabarraga, and R. Adhikari, *Lattice-Boltzmann–Langevin simulations of binary mixtures*, Phys. Rev. E **84** (2011), 046709.

[72] C. J. Takacs, G. Nikolaenko, and D. S. Cannell, *Dynamics of long-wavelength fluctuations in a fluid layer heated from above*, Phys. Rev. Lett. **100** (2008), no. 23, 234502.

[73] F. B. Usabiaga, J. B. Bell, R. Delgado-Buscalioni, A. Donev, T. G. Fai, B. E. Griffith, and C. S. Peskin, *Staggered schemes for fluctuating hydrodynamics*, Multiscale Model. Simul. **10** (2012), no. 4, 1369–1408. MR 3022043 Zbl 06160065

[74] A. Vailati, R. Cerbino, S. Mazzoni, M. Giglio, C. J. Takacs, and D. S. Cannell, *Gradient-driven fluctuations in microgravity*, J. Phys. Condens. Matter **24** (2012), no. 28, 284134.

[75] A. Vailati, R. Cerbino, S. Mazzoni, C. J. Takacs, D. S. Cannell, and M. Giglio, *Fractal fronts of diffusion in microgravity*, Nat. Commun. **2** (2011), 290.

[76] A. Vailati and M. Giglio, *Giant fluctuations in a free diffusion process*, Nature **390** (1997), 262–265.

[77] ———, *Nonequilibrium fluctuations in time-dependent diffusion processes*, Phys. Rev. E **58** (1998), no. 4, 4361–4371.

[78] N. K. Voulgarakis and J.-W. Chu, *Bridging fluctuating hydrodynamics and molecular dynamics simulations of fluids*, J. Chem. Phys. **130** (2009), no. 13, 134111.

[79] L. Wang and M. Quintard, *Nanofluids of the future*, Advances in transport phenomena 2009 (L. Wang, ed.), Adv. Trans. Phenom., no. 1, Springer, Berlin, 2009, pp. 179–243.

Received November 26, 2013. Revised January 14, 2014.

ALEKSANDAR DONEV: donev@courant.nyu.edu
Courant Institute of Mathematical Sciences, New York University, 251 Mercer Street, New York, NY 10012, United States

ANDY NONAKA: ajnonaka@lbl.gov
Center for Computational Sciences and Engineering, Lawrence Berkeley National Laboratory, 1 Cyclotron Road, Berkeley, CA 94720, United States

YIFEI SUN: yifei@cims.nyu.edu
Courant Institute of Mathematical Sciences, New York University, 251 Mercer Street, New York, NY 10012, United States

and

Leon H. Charney Division of Cardiology, Department of Medicine, New York University School of Medicine, New York, NY 10016, United States

THOMAS G. FAI: tfai@cims.nyu.edu
Courant Institute of Mathematical Sciences, New York University, 251 Mercer Street, New York, NY 10012, United States

ALEJANDRO L. GARCIA: alejandro.garcia@sjsu.edu
Department of Physics and Astronomy, San Jose State University, 1 Washington Square, San Jose, CA 95192, United States

JOHN B. BELL: jbbell@lbl.gov
Center for Computational Sciences and Engineering, Lawrence Berkeley National Laboratory, 1 Cyclotron Road, Berkeley, CA 94720, United States